ChemistryEurope
Excellence in Chemistry Research Worldwide

Research Article
doi.org/10.1002/ceur.202300012

www.journal.chemistry-europe.org

Complexities of the Interaction of Ni^{II}, Pd^{II} and Pt^{II} Pyrrole-Imine Chelates with Human Serum Albumin**

Sheldon Sookai[a] and Orde Q. Munro*[a, b]

Dedicated to Professor Helder M. Marques

Human serum albumin (HSA) efficiently transports drugs in vivo: most are organic. Here, HSA binding affinity and site specificity are shown to depend on the identity of the d^8 metal ion in Ni^{II}, Pd^{II} and Pt^{II} chelates of the bis(pyrrole-imine) ligand H_2PrPyrr. Fluorescence quenching data for native and probe-bound HSA showed sites close to Trp-214 (subdomain IIA) are targeted. The Stern-Volmer constants, K_{SV}, ranged from $10^4\ M^{-1}$ to $10^5\ M^{-1}$ while the affinity constants, K_a, ranged from $\sim 3.5\times10^3\ M^{-1}$ to $\sim 1\times10^6\ M^{-1}$ at 37 °C, following the order Pd(PrPyrr) > Pt(PrPyrr) > Ni(PrPyrr) > H_2PrPyrr. Ligand uptake is enthalpically driven, hinging mainly on London dispersion forces. Induced CD spectra for the protein-bound ligands could be simulated by hybrid QM:MM TD-DFT methods, proving that the metal chelates neither decompose nor demetallate after uptake by HSA. Transport and delivery of the metal chelates by HSA in vivo could therefore be feasible.

Introduction

Pyrrole-based compounds have been extensively studied due to their intrinsic bioactivity and use in pharmaceuticals.[1,2] Pyrrole-imine Schiff bases are popular ligands formed by condensing pyrrole-2-carboxaldehyde with primary alkyl- or arylamines.[3] The resulting pyrrole-imine Schiff bases chelate numerous metal ions, forming stable complexes with metal–pyrrolide and metal-imine bonds after concomitant deprotonation of the pyrrole NH group. When suitable diamines are condensed with two mole equivalents of the carbonyl synthon, tetradentate bis(pyrrole-imine) Schiff base ligands are obtained (Figure 1a), and hexadentate derivatives may be similarly prepared.[4–6] Such ligands stabilize metal ions in a range of oxidation states.[7] Examples include structurally characterized $Co^{II/III}$,[8–11] $Rh^{I/III}$,[12–15] Ir^{III},[16,17] Ni^{II},[18–20] Pd^{II},[20–22] Pt^{II},[23–25] Cu^{II},[26–29] Ag^{I},[30] and Au^{III} complexes.[31]

While pyrrole compounds are key building blocks for organic pharmaceuticals,[32] for example, Tolmetin,[33] Sunitinib,[34] and Glimepiride,[35] studies over the last two decades suggest that pyrrole-imine metal chelates exhibit significant medicinal potential. The best-known example is the pentadentate macrocycle texaphyrin,[36] which complexes numerous transition and main group metal ions, including lanthanides. Texaphyrin's Lu^{III}[37] and Gd^{III}[38] complexes are promising (but not FDA-approved) compounds for photodynamic cancer chemotherapy[39] and MRI contrast[40] applications, respectively. Although further behind on the clinical development trajectory, patented tetradentate bis(pyrrolide-imine) chelates of Au^{III} are promising investigational compounds for cancer[31] and mycobacterial chemotherapy.[41] Despite these advances, limited work has been done to elucidate how these compounds bind to human serum albumin (HSA), which is critical to understanding the plasma distribution of metal chelate drug candidates.[42] In this paper, our primary aim was to use simple pyrrole-imine metal chelates to study their uptake by HSA in order to better understand whether HSA might potentially serve as a transporter/delivery vehicle for such compounds in vivo.

HSA is the most abundant plasma protein present at concentrations of around 600 μM.[43] Two of the main functions of HSA are regulating colloidal osmotic pressure and transportation of exogenous and endogenous compounds.[44] HSA is a heart shaped macromolecule that consists of a single polypeptide chain (585 amino acids) with a molar mass of 66.5 kDa.[45] As depicted in Figure 1b, the structure is dominated by α-helices within the three domains, namely I (residues 1–195), II (196–383), and III (384–585). Each domain is further broken down into two subdomains A and B.[45,46] The two main small molecule binding sites within HSA are in subdomains IIA and IIIA and are often referred to as Sudlow's site I and Sudlow's site II, respectively.[47–49] HSA is the quintessential drug transporter in humans and is thus widely studied as a potential vehicle for drug delivery, especially since the protein is assimilated by cancer cells in vivo.[50] Apart from the two main drug binding sites, other binding sites abound, including 7 fatty acid, 4 thyroxine, and several known metal ion binding sites.[51]

[a] S. Sookai, Prof. Dr. O. Q. Munro
Molecular Sciences Institute
School of Chemistry
University of the Witwatersrand,
PO WITS 2050, Johannesburg (South Africa)
[b] Prof. Dr. O. Q. Munro
School of Chemistry
University of Leeds,
Woodhouse Lane, LS2 9JT, Leeds (UK)
E-mail: o.munro@leeds.ac.uk

[**] A previous version of this manuscript has been deposited on a preprint server (https://chemrxiv.org/engage/chemrxiv/article-details/63e4dac7fcfb27a31f735a11).

Supporting information for this article is available on the WWW under https://doi.org/10.1002/ceur.202300012

Research Article
doi.org/10.1002/ceur.202300012

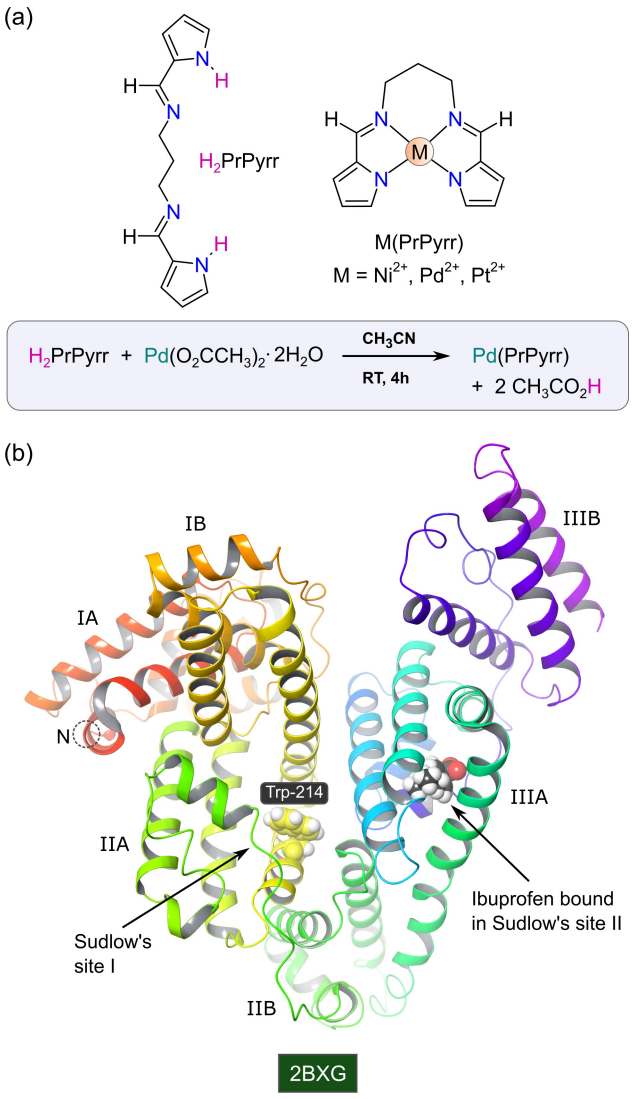

Figure 1. (a) Structures of the bis(pyrrole-imine) ligand $H_2PrPyrr$ (*N,N′-bis*[(1*E*)-1H-pyrrol-2-ylmethylene]propane-1,3-diamine) and its neutral metal chelates with square planar d^8 metal ions relevant to this work. The method for metalation of the ligand is illustrated for the synthesis of Pd(PrPyrr); the solvate water molecules enter the bulk solvent. (b) X-ray structure of HSA bound to ibuprofen (redrawn from PDB code 2BXG) illustrating the two main small molecule binding sites. Sudlow's site I is larger than Sudlow's site II and compounds that bind in this pocket perturb the fluorescence from Trp-214. The protein secondary structure elements are depicted schematically, coloured by domain, and labelled with Roman numerals and Arabic letters. H atoms (calculated positions) were added to the bound drug and Trp-214 to enhance their visualization.

Delineating the binding of a medicinal compound to HSA is central to understanding its pharmacodynamic and pharmacokinetic data in vivo given the abundance of HSA and its transporter role in blood plasma.[47] Metallodrug candidates are no exception and recent work has shown how half-sandwich Ru^{II} and Rh^{III} complexes bind to HSA as intact species through coordination to His and Glu residues with retention of the arene.[52–54] Generally, protein binding by metal complexes is accompanied by ligand dissociation[55–58] while non-dissociative binding is less common,[59–62] often though not exclusively[63] hinging on multidentate ligands that provide kinetic inertness and thermodynamic stability.[64,65] For instance, large substitution-inert mono- and multinuclear Ru^{II} complexes with bidentate ligands such as bipy (2,2′-bipyridine), phen (1,10-phenanthroline), and dppz (dipyridophenazine) are taken up by HSA ostensibly as fully intact species, often with stoichiometries ≥ 1, attesting to the promiscuity of HSA and its affinity for diverse, structurally elaborate compounds.[66–68]

Here, we synthesized a popular tetradentate *bis*(pyrrole-imine) ligand, $H_2PrPyrr$, and its isoelectronic (nd^8) square-planar chelates of Ni^{II}, Pd^{II}, and Pt^{II}, denoted M(PrPyrr) (Figure 1a). Spectroscopic methods were used to probe the binding of $H_2PrPyrr$ and M(PrPyrr) by HSA under physiological conditions to gauge how the metal ion influences uptake of the complexes and to delineate their preferred binding site(s). For the first time, we show that the binding affinity, thermodynamics, and practically all aspects of the physical biochemistry of the system are surprisingly sensitive to the identity of the nd^8 metal ion. Notwithstanding the complexity of the system, we have shown that the protein binds the fully intact metal chelates. $H_2PrPyrr$ and M(PrPyrr) are thus stable to hydrolysis and demetallation, respectively, during uptake and binding by the protein. This is particularly important because of the general apathy displayed by pharmaceutical companies towards the development of metallodrugs.

Results and Discussion

Metal chelate synthesis

Modified literature methods were used to metalate $H_2PrPyrr$ with Ni^{II}[69] and Pt^{II}.[70] For Pt(PrPyrr), simply stirring the solution of the free ligand with $K_2[PtCl_4]$ and sodium acetate in a binary mixture of DMSO-acetonitrile (50 %, V/V) for 4 days at ambient temperature (as opposed to the 4-h reaction at 80 °C in DMF employed for the cyclohexyl-bridged ligand[70]) afforded the product cleanly without formation of metal-containing by-products. The difference in reactivity of $H_2PrPyrr$ towards Pt^{II} compared with the cyclohexyl-bridged ligands likely reflects the higher flexibility of the propyl-bridged analogue employed here. For Pd(PrPyrr), the protocol depicted in Figure 1a was followed with the use of Pd^{II} acetate affording the product cleanly; the free acetate ions serve as a suitable base for accepting the pyrrole NH protons released during metal ion chelation. We found it unnecessary to first dissolve the free ligand in ethanol, as reported elsewhere for this reaction, obviating the need for a mixed solvent system.[71]

Adventitious formation of PdCl(HPrPyrr)

For Pd(PrPyrr), protonation of the metal-bound ligand was discovered and the species found to be significant for uptake by HSA (see below). More specifically, the tridentate hemi-protonated complex PdCl(HPrPyrr) was unexpectedly obtained from a reaction in which Pd(PrPyrr) had been synthesized as

Research Article
doi.org/10.1002/ceur.202300012

depicted in Figure 1a. The crystals which grew from a mixture of CH_2Cl_2 and hexane were heterogeneous comprising Pd(PrPyrr) as the majority species and PdCl(HPrPyrr) as a minor component. The source of chloride ions for the latter reaction product may derive from the commercial solvent[72] or the hydrolysis of CH_2Cl_2 to form HCl and formaldehyde (Scheme 1),[73] possibly catalysed by residual acetic acid present as a by-product of the metalation of H_2PrPyrr with $Pd(O_2CCH_3)_2$. Protonation of coordinated N-donor ligands in Pd^{II} pincer complexes is known and can be achieved by simply using HCl•OEt_2 to effect the reaction.[74]

Here, experimental evidence in support of the mechanism depicted in Scheme 1 was acquired by investigating the reactions of Pd(PrPyrr) and H_2PrPyrr with HCl using UV-visible and ^{1}H NMR spectroscopy. As shown in Figure 2a, progressively increasing the concentration of HCl in an acetonitrile solution containing 20 μM Pd(PrPyrr) converts the complex into the protonated adduct PdCl(HPrPyrr). A significant excess of HCl was required to bring about complete reaction. Notably, from the spectra of the free ligand (H_2PrPyrr) recorded as a function of [HCl] (Figure 2b), addition of HCl to Pd(PrPyrr) does not lead to demetallation of the chelate and hence formation of the protonated fee base, either $[H_3PrPyrr]^+$ or $[H_4PrPyrr]^{2+}$. The species assignments above were confirmed by the TD-DFT spectra of Pd(PrPyrr) and PdCl(HPrPyrr) calculated in acetonitrile (Figure S13), which show remarkably good agreement with the experimental spectra.

Since the structural hallmark of PdCl(HPrPyrr) is its lack of symmetry and a single protonated pyrrole group, the ^{1}H NMR spectrum of Pd(PrPyrr) before and after addition of 2 equiv. HCl in CD_3CN confirmed the appearance of two new, moderately sharp signals at 8.12 and 8.21 ppm, which may be assigned to the pyrrole NH proton and imine CH proton of the chelate closest to the protonated pyrrole ring. Both exhibit exchange broadening. In contrast, the imine CH proton signal of the coordinated pyrrolide-imine moiety is sharp and resonates downfield (8.03 ppm) relative to the parent complex (7.70 ppm). The spectrum of Pd(PrPyrr) recorded in acidified acetonitrile is thus consistent with the structure of PdCl(HPrPyrr). The remaining signals for the protonated complex were in excellent agreement with those calculated by DFT methods (Figure S14). From Figure 2, an additional minor species of a similar structure to PdCl(HPrPyrr) is present (signals

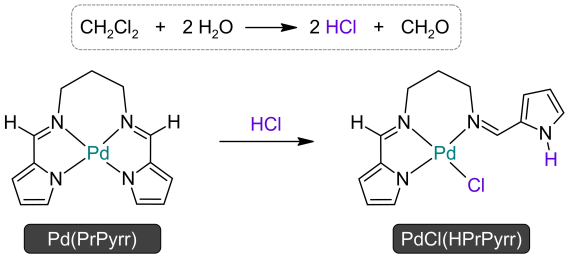

Scheme 1. Conversion of Pd(PrPyrr) to the protonated tridentate chloro adduct, PdCl(HPrPyrr), by HCl derived from a postulated solvent decomposition reaction.

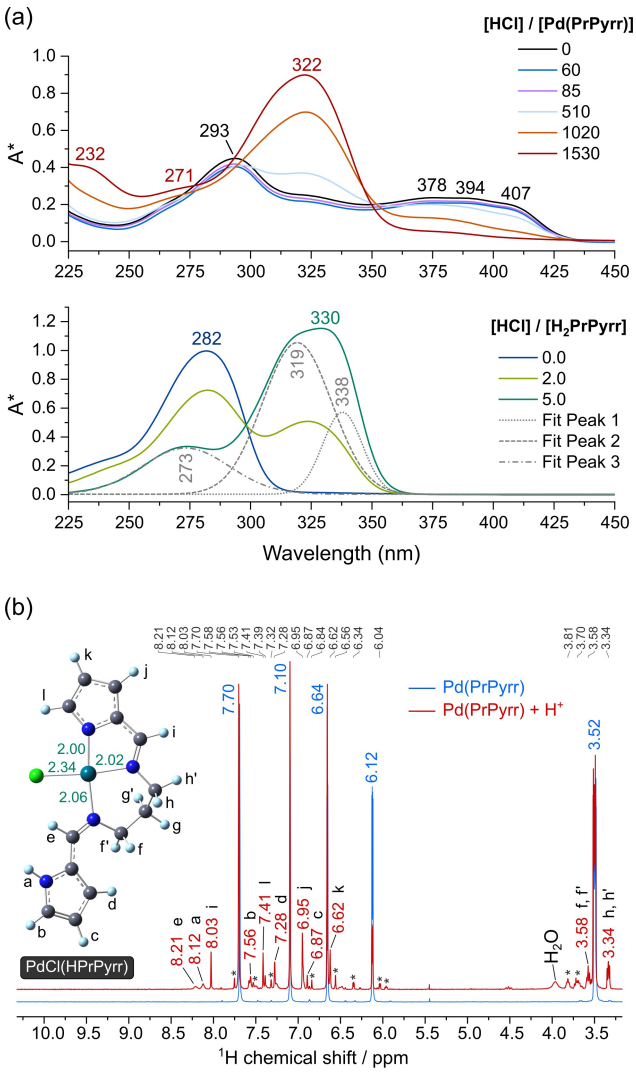

Figure 2. (a) Protonation of Pd(PrPyrr) and H_2PrPyrr studied by UV-visible spectroscopy in acetonitrile solution at 37 °C. The spectra were smoothed with an FFT filter algorithm (5-point window, OriginPro 2021). The electronic spectrum of the protonated free base ligand, $[H_4PrPyrr]^{2+}$, was deconvoluted into three Gaussian bands (fit $R^2 = 0.998$, $\chi^2 = 1.6 \times 10^{-4}$). There are no bands below 250 nm or above 350 nm. (b) ^{1}H NMR spectra of Pd(PrPyrr) recorded in CD_3CN in the absence (blue) and presence (red) of 2 equiv. of HCl in D_2O recorded at 37 °C. The DFT-calculated structure of PdCl(HPrPyrr) is shown along with signal assignments in the experimental NMR spectrum that are based on the isotropic shielding tensors calculated for the protons in the complex. DFT-calculated bond distances are in Å. The signal from the central methylene group of the propyl bridge (not shown) is overlapped with the solvent peaks at 1.97 ppm (see Figure S2). The minor signals marked with an asterisk possibly belong to the solvated complex (Cl^- exchange).

marked with an asterisk), possibly the solvent-substituted salt $[Pd(HPrPyrr)(NCCH_3)]Cl$. Since two CH_2-group resonances occur at 3.70 and 3.81 ppm for this minor species, we can rule out double-protonation of Pd(PrPyrr) as this would lead to either dissociation of the ligand from the Pd^{II} ion or formation of a symmetric structure with metal-coordination by the central chelate ring alone (i.e., there would be two dissociated pyrrole rings). Both options would give a single methylene resonance in this region of the spectrum, inconsistent with the exper-

Research Article
doi.org/10.1002/ceur.202300012

imental data. Collectively, the UV-visible and NMR spectroscopic data strongly support the mechanism proposed in Scheme 1.

X-ray structures of Pd(PrPyrr) and PdCl(HPrPyrr)

The ambient temperature X-ray structure of Ni(PrPyrr) has been previously described.[69] The novel low temperature X-ray structures of Pd(PrPyrr) and PdCl(HPrPyrr) delineated here are shown in Figure 3. Pd(PrPyrr) crystallized in the space group $P2_1/c$ (Table S1, Figure S15) and is structurally similar to the room temperature X-ray structure of the compound (Figure S16).[71] The asymmetric unit (ASU) for Pd(PrPyrr) comprises four independent molecules (A–D), each having the square planar Pd^{II} ion chelated by the tetradentate bis(pyrrolide-imine) ligand. The Pd–$N_{pyrrole}$ and Pd–N_{imine} distances average 2.017(6) and 2.010(11) Å, respectively (Table S2). These bond distances are statistically equivalent to the mean Pd–$N_{pyrrole}$ and Pd–N_{imine} values of 2.02(3) Å and 2.02(4) Å, respectively, calculated from 27 similar structures in the Cambridge Crystallographic Database (CSD).[75] The literature data are collated in Table S3 and plotted in Figure S17. Interestingly, despite the higher temperature data for the literature structure of PdPrPyrr,[71] which has mean Pd–$N_{pyrrole}$ and Pd–N_{imine} distances of 2.011(4) and 2.006(10) Å, respectively, the coordination group bonds are equivalent (within 1σ) to those determined here at 173 K. The nonplanar conformations of the ligands mainly reflect non-bonded crystal packing interactions and the formation of discrete π-stacked dimers (see Figure S18). Notably, DFT simulations (Figure S19) suggest the observed stacking involves significant London dispersion forces.

The X-ray structure of PdCl(HPrPyrr) is shown in Figure 3b. The square planar Pd^{II} ion is chelated by three of the four nitrogen donors of the monoanionic tetradentate chelate, with the protonated pyrrole ring unbound and oriented away from the chloride ligand occupying the fourth coordination site at the metal ion. The unbound pyrrole N–H group participates in intermolecular N–H···Cl hydrogen bonding (2.40 ± 0.02 Å), which leads to the formation of a one-dimensional H-bonded chain in the solid state. The polymer chain axis is colinear with the lattice 2-fold screw axis, giving the extended chain 2_1 symmetry overall (Figure S20). The Pd–$N_{pyrrole}$ and mean Pd–N_{imine} distances measure 1.993(1) and 2.015(18) Å, respectively. The individual Pd–N_{imine} bond distances, measuring 1.997(1) and 2.032(1) Å, vary significantly depending on whether the flanking pyrrole ring is metal-bound or not. The shorter distance (Pd1–N2) occurs when the pyrrole ring is metal-bound, and the imine nitrogen resides within the 5-membered chelate ring incorporating the metal ion. This reflects the binding constraints imposed by the 5-membered chelate ring on N2, which are relaxed for N3 within the larger 6-membered chelate ring (propyl bridge). The Pd–Cl distance measures 2.3204(4) Å and is typical for coordination of Pd^{II} by chloride in pyrrole-based pincers.[74] Interestingly, there are no X-ray structures for comparison with PdCl(HPrPyrr) in the literature, commensurate with the unusual nature of this species.

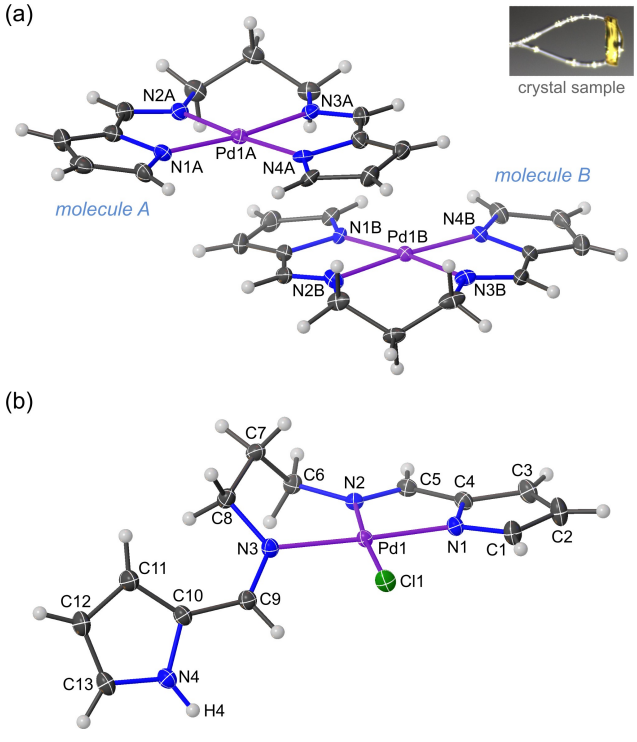

Figure 3. (a) Partly labelled view of the low-temperature X-ray structure of Pd(PrPyrr). Two of the four independent molecules (A and B) in the asymmetric unit are illustrated. (b) View of the low temperature X-ray structure of PdCl(HPrPyrr). Thermal ellipsoids are rendered at the 35% and 50% probability levels for Pd(PrPyrr) and PdCl(HPrPyrr), respectively. Hydrogen atoms are drawn as spheres with an arbitrary radius.

Ligand-dependent HSA fluorescence quenching

To delineate the mechanism and relative ability of H_2PrPyrr and its M(PrPyrr) chelates to interact with HSA, fluorescence spectroscopy was used as an informative probe. Specifically, fluorescence quenching for a protein can be described as either static, dynamic, or a combination of both. For HSA, the intrinsic fluorescence emission is largely the result of a single tryptophan residue (Trp-214, $\lambda^{ex} = 280$ nm) located in subdomain IIA, and to a lesser extent the 18 tyrosine residues present in the protein.[76] Emission quenching of HSA induced by varying concentrations of the free ligand, H_2PrPyrr, and its Group 10 d^8 M(PrPyrr) chelates (Figures 4 and S23) was characterized by a monotonic intensity decrease at the emission maximum (~343 nm) with increasing [L]. (Here, ligand L is used in a biomolecular sense.) The spectroscopic data suggest that all four ligands bind reasonably close to Trp-214 (subdomain IIA), changing the microenvironment around the fluorophore and inducing a marked dose-dependent (i.e., "static" or binding-related) quenching of the intrinsic fluorescence of HSA (see below).[77,78]

For HSA, the wavelength of the fluorescence emission maximum (λ^{em}_{max}) was dependent on the identity of the bound ligand. At the maximum doses investigated before quenching and band broadening limited fluorescence detection, H_2PrPyrr and Pd(PrPyrr) induced blue shifts relative to the native protein

Research Article
doi.org/10.1002/ceur.202300012

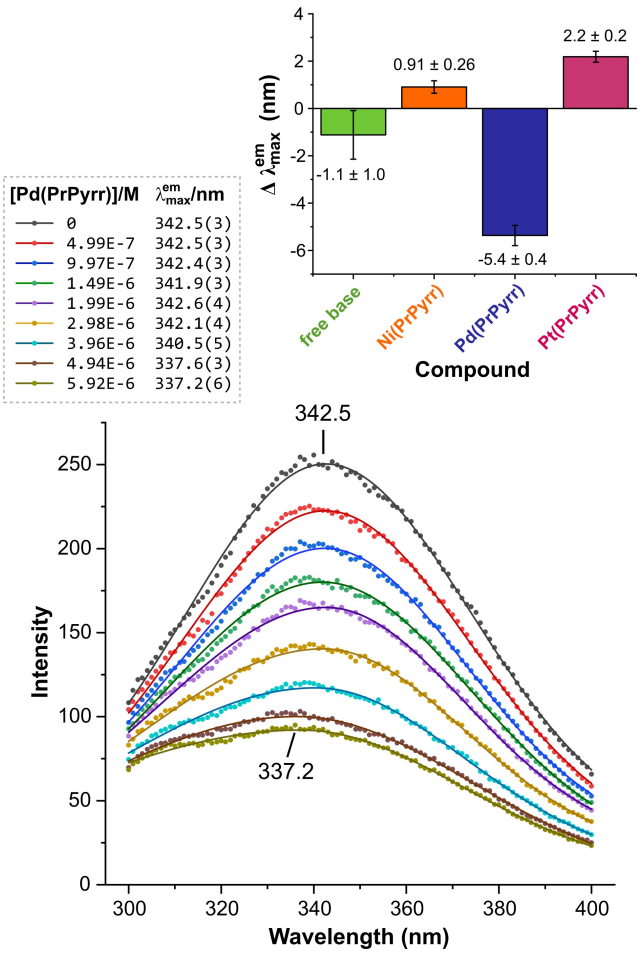

Figure 4. Emission spectra of human serum albumin (HSA, 5.0 μM) recorded as a function of the concentration of Pd(PrPyrr) at 298 K (pH 7.50). The spectra are fitted by paired asymmetric Gaussian functions to locate the emission maxima. Correlation coefficients, R^2, were all 0.997. Analogous spectra for the reaction of HSA with H_2PrPyrr, Ni(PrPyrr), and Pt(PrPyrr) are given in Figure S23 (Supporting Information). The wavelength shift accompanying ligand uptake ($\Delta\lambda^{em}_{max}$) is plotted as the inset to the main figure (upper right).

of -1.1 ± 1.0 and -5.4 ± 0.4 nm, respectively (identical buffer and temperature). In contrast, the Ni^{II} and Pt^{II} chelates red-shifted λ^{em}_{max} by up to $+2.2\pm0.2$ nm in the case of the Pt^{II} derivative. While shifts of ~1 nm in λ^{em}_{max} are close to the wavelength resolution of the instrument (i.e., statistically insignificant), the notable blue shift in the emission maximum for Pd(PrPyrr) ostensibly reflects the development of a significantly less polar environment around Trp-214 after ligand uptake.[79,80] From the Hill-type function[81] used to fit the variation in HSA emission wavelength with [Pd(PrPyrr)] (Figure S24), the wavelength shift is ~99% complete when [Pd(PrPyrr)] = 6 μM.

The magnitude of the blue shift in λ^{em}_{max} for Trp observed here for the HSA·{Pd^{II}} system (relative to native HSA) is akin to that found for many other proteins (where λ^{em}_{max} ranges from 308 nm to 365 nm, but is most commonly 330–340 nm).[82] A blue shift in λ^{em}_{max} for Trp is usually caused by changes in (i) the orientational polarization of the Trp fluorophore induced by ordered water molecules within 15–25 Å of the residue and (ii) electronic polarization of the Trp indole ring. For HSA·{ligand} complexes, electronic polarization of Trp-214 induced by the bound ligand and perturbation of the ordered water structure around the fluorophore both likely underpin the observed shifts in λ^{em}_{max}. Whether a blue or red shift in λ^{em}_{max} occurs depends on the orientation and centre-to-centre distance of the ligand's dipole moment relative to the transition dipole moment for the lowest energy $^1A_1\rightarrow{}^1L_a$ ground state transition of Trp's indole ring.[79] (This transition involves pyrrole→benzene transient charge migration.) Hence, the precise way in which the ligand is bound relative to Trp-214 will govern the sign and magnitude of $\Delta\lambda^{em}_{max}$.

The red shift in $\Delta\lambda^{em}_{max}$ of $+2.2\pm0.2$ nm for HSA·{Pt(PrPyrr)} suggests that the environment around Trp-214 becomes somewhat more hydrophilic (polar) upon ligand uptake,[80] possibly reflecting rearrangement of the positions or orientations of H-bonded water molecules within a 15–25 Å radius of Trp-214. (Even though Trp and Tyr are readily excited at 280 nm, most of the intrinsic fluorescence of HSA is due to Trp-214 since it has a higher quantum yield and more efficient resonance energy transfer than Tyr;[76] see Table S6.) The key conclusion from the wavelength shift data is that the Pd^{II} system probably binds to HSA in a different manner to the Ni^{II} and Pt^{II} analogues.

Fluorescence quenching mechanism

Stern-Volmer (SV) plots of the mean fluorescence ratio recorded as a function of ligand dose are presented in Figures 5 and S25. (SV quenching theory is provided in Eqs. S3 and S4 of the Supporting Information) The calculated SV constants, K_{SV}, and bimolecular quenching rate constants, k_q, for the interaction of the four ligands with HSA are given in Table 1. The K_{SV} values all decrease with increasing temperature and the k_q values exceed the diffusion-controlled limit (1×10^{10} $M^{-1}s^{-1}$)[83] by 2 to 3 orders of magnitude, consistent with stable complex formation and a static fluorescence quenching mechanism (binding related). The values of K_{SV} and k_q determined here for the interaction of native HSA with H_2PrPyrr and its metal chelates are from ~2 to ~10 times larger than, for instance, those reported for HSA interacting with berberine,[84] epinastine hydrochloride,[85] primethamine and trimethoprim,[86] as well as malvidin-3-glucoside.[87]

Ligand binding equilibrium constants

To investigate metal complex integrity and affinity for HSA, we employed the changes in HSA fluorescence intensity as a function of ligand dose to calculate thermodynamic data for the binding equilibrium between the protein and titrant ligand. The biophysical parameters (Table 1) that describe the ligand's affinity for the protein (K_a) and the reaction stoichiometry (n) are delineated from a double-log plot (Figures 5b and S26) of the emission data as a function of increasing ligand concentration [Equation (1)],[88]

Research Article
doi.org/10.1002/ceur.202300012

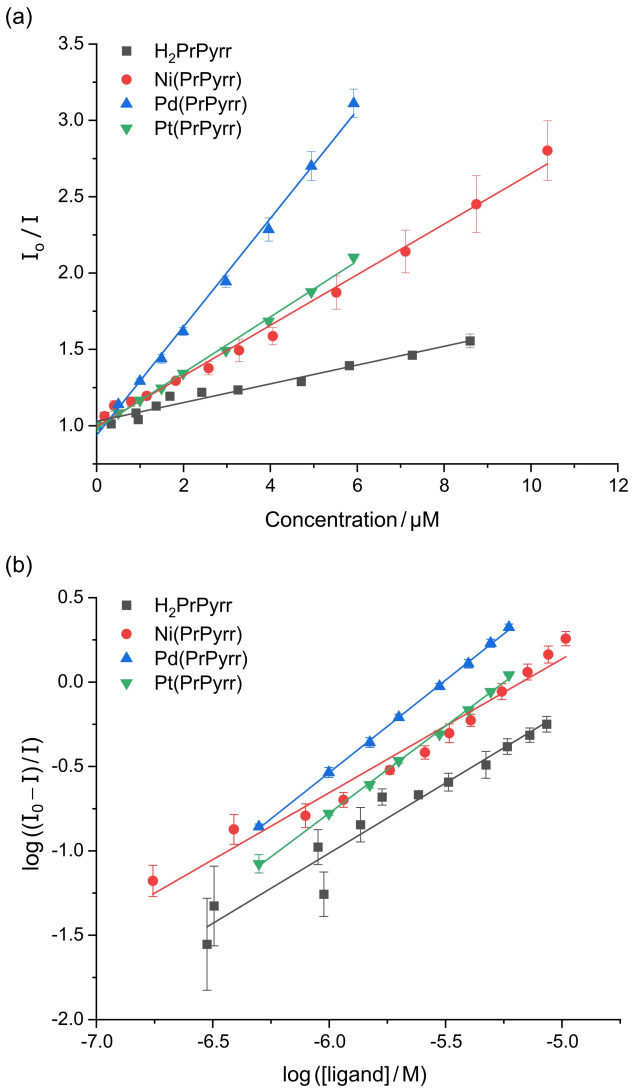

Figure 5. (a) Stern-Volmer (SV) fluorescence intensity ratio plots for human serum albumin (HSA, 5.0 μM) recorded as a function of the concentration of H_2PrPyrr, Ni(PrPyrr), Pd(PrPyrr), and Pt(PrPyrr) in 50 mM KH_2PO_4, pH 7.50, at 298 K. All data are well-fitted by Equation S3 for linear SV emission behaviour with appreciable static quenching. (b) Double logarithm plot of the fractional change in fluorescence intensity for human serum albumin (HSA, 5.0 μM) recorded as a function of the concentration of H_2PrPyrr, Ni(PrPyrr), Pd(PrPyrr), and Pt(PrPyrr) in 50 mM KH_2PO_4, pH 7.50, at 298 K. The data are described by Equation (1), which affords the affinity constant and stoichiometric coefficient for the reaction (Table 1). For both plots, error bars are estimated standard deviations based on the average of three independent determinations.

$$log\left(\frac{I_0 - I}{I}\right) = logK_a + nlog[Q] \quad (1)$$

where the intercept and slope of the curve give the affinity constant and stoichiometry, respectively. For each compound, K_a decreases with increasing temperature, consistent with a static quenching mechanism.[89,90] The stoichiometric coefficients n obtained for Pd(PrPyrr) were >1 (e.g., 1.19±0.01 at 288 K), suggesting that the reaction stoichiometry might entail the uptake of two metal chelates (2:1 ligand:HSA) with fractional occupancy of the target binding sites. The behaviour

Table 1. Stern-Volmer quenching constants (K_{SV}), bimolecular quenching rate constants (k_q), association constants (K_a) and stoichiometric coefficients (n) for the interaction of H_2PrPyrr, Ni(PrPyrr), Pd(PrPyrr) and Pt(PrPyrr) with HSA at different temperatures in 50 mM KH_2PO_4 buffer at pH 7.50.

Compound	T [K]	10^{-5} K_{SV} [M^{-1}][a,c]	10^{-13} k_q [$M^{-1}s^{-1}$][b]	log(K_a / M^{-1})[c]	n[d]
H_2PrPyrr	288	2.12 (3)	3.61	4.04 (14)	0.76 (2)
	298	0.61 (4)	1.04	3.55 (9)	0.76 (2)
	310	0.47 (5)	0.78	2.56 (5)	0.55 (4)
Ni(PrPyrr)	288	1.69 (20)	2.88	5.15 (21)	0.97 (2)
	298	1.55 (10)	2.64	4.63 (14)	0.89 (2)
	310	1.21 (4)	2.10	4.39 (13)	0.88 (2)
	315	1.18 (4)	2.01	3.22 (14)	0.64 (2)
Pd(PrPyrr)	288	4.60 (30)	7.81	6.68 (6)	1.19 (1)
	298	3.60 (20)	6.04	6.00 (7)	1.08 (1)
	310	2.52 (10)	4.30	5.52 (17)	1.01 (2)
	315	2.10 (10)	3.52	5.28 (3)	0.99 (0)
Pt(PrPyrr)	288	2.12 (10)	3.61	5.69 (6)	1.05 (4)
	298	1.83 (1)	3.11	5.34 (18)	1.02 (3)
	310	1.34 (5)	2.28	5.23 (13)	1.02 (2)
	315	1.12 (5)	1.91	4.95 (6)	0.98 (1)

[a] K_{SV} values (Stern-Volmer constants) were determined from fitting the data to Equation (S3). [b] Using Equation (S4), a mean excited state lifetime, τ_0, of 5.87(76) ns for HSA was used to calculate the bimolecular quenching rate constants, k_q. [c] The estimated standard deviations of the least significant digits are given in parentheses. [d] Ligand:HSA binding stoichiometry.

of Pd(PrPyrr) with HSA contrasts that for H_2PrPyrr (n = 0.76 ± 0.02 at 288 K) and Ni(PrPyrr) (n = 0.97 ± 0.02 at 288 K), since these compounds had sharply varying reaction stoichiometries (and consequently binding site occupancies) over the temperature range investigated.

From Table 1, the $logK_a$ values follow the order Pd(PrPyrr) ≫Pt(PrPyrr) > Ni(PrPyrr) > H_2PrPyrr. Notably, the value of $logK_a$ for the Pd^{II} chelate ranges from 6.68–5.28 (288–315 K) and is akin to the product equilibrium constant β_2, where $log\beta_2 = logK_1 + logK_2$, accounting for why the affinity constant is an order of magnitude larger than the K_a values measured for the Pt^{II} or Ni^{II} congeners. Significantly, K_1 and K_2 for the reaction of HSA with the Pd^{II} system are *unresolvable*, reflecting concurrent ligand binding. Since the isostructural neutral metal chelates Ni(PrPyrr) and Pt(PrPyrr) are similar, and neither readily undergo ligand exchange, it is expected that they will bind noncovalently to the same site in HSA with the affinity of Pt(PrPyrr) exceeding that of Ni(PrPyrr) due to enhanced London dispersion forces of attraction engendered by the electron-rich Pt^{II} ion. The logK_a values fall in the range 5.69–3.22 (288–315 K) for these chelates.

Reaction mechanism and binding site specificity

Pd^{II} chelate hydrolysis underpins its reaction with HSA. A feasible reaction for Pd(PrPyrr), given its lability and solution chemistry (Scheme 1, Figure 2), is hydrolysis of the complex to form the aqua species, Equation (2):

$$Pd(PrPyrr) + H_3O^+ \rightleftharpoons [Pd(HPrPyrr)(OH_2)]^+ \quad (2)$$

Research Article
doi.org/10.1002/ceur.202300012

This reaction occurs spontaneously in solution and only for the Pd^{II} chelate. Therefore, *two* Pd^{II} species are present to react with HSA and, because they are structurally distinct, will likely bind in two independent sites within range of Trp-214 to collectively quench its fluorescence. Experimental evidence for the spontaneous formation of $[Pd(HPrPyrr)(OH_2)]^+$ was obtained by measuring the time-dependent electronic absorption and circular dichroism (CD) spectra of Pd(PrPyrr) in aqueous solution. The amplitude of the absorption spectrum of Pd-(PrPyrr) decreases with increasing time, reflecting first-order kinetics and formation of $[Pd(HPrPyrr)(OH_2)]^+$ (within ~40 min, Figures S21 and S22). The time-dependent CD spectra are shown in Figure S28a along with the DFT-calculated spectrum of this species. Because Pd(PrPyrr) has exact *Cs* symmetry it has no CD spectrum. The structure of $[Pd(HPrPyrr)(OH_2)]^+$, in contrast, has C_1 symmetry with enantiomers that differ in energy by ~50 kcal mol^{-1}, thwarting racemization. The chiral hydrolysis product thus has a distinct CD spectrum that is easily measured upon its formation. Regarding the species distribution as a function of pH, the aqua complex $[Pd(HPrPyrr)(OH_2)]^+$ is prevalent over the pH range 5.5–7.5 ($pK_2 = 8.37 \pm 0.04$) while the transition to the chloro derivative at low pH, PdCl(HPrPyrr), occurs with $pK_1 = 4.62 \pm 0.06$ (Figure S28b). Notably, the equilibrium mixture at any pH always contains from 47 to 62% Pd(PrPyrr), as evidenced by the complexity of the UV-visible spectra (Figure S28c).

Probe displacement assays delineate the main Pd^{II} binding sites. To understand how the species distribution in Equation (2) affects the reaction of the Pd^{II} system with HSA, we carried out a competitive blocking assay in which the ligand was titrated into solutions of both native HSA and solutions that were pre-equilibrated with (i) warfarin and (ii) ibuprofen (Figure 6). As revealed by X-ray crystallography, warfarin binds specifically in Sudlow's site I (subdomain IIA),[91] while ibuprofen primarily binds in Sudlow's site II (subdomain IIIA), with a secondary site in the region between subdomains IIA and IIB (IIA-IIB).[92] By selectively and sequentially blocking the two main drug binding sites of HSA, the experiment can potentially delineate a ligand's binding site specificity. One caveat is that HSA has multiple drug binding sites.[92] Blocking a primary binding site may redirect ligand uptake to a secondary binding site within the protein (or thwart incoming ligand binding by allosteric inhibition). However, changes in the affinity constant, stoichiometry, K_{SV}, and substitution of the blocking drug itself might occur, thereby revealing a possible binding site for the ligand. The system is intricate, but we have summarized the experimental strategy used and the results obtained pictorially in Figure 7 (which also incorporates our in silico binding site affinity data, see below).

For brevity, uptake of the Pd^{II} species by HSA is discussed here; the remaining ligands are simpler to understand and are analysed in the Supporting Information (Figures S30–S32). When the equilibrium mixture of Pd(PrPyrr) and $[Pd(HPrPyrr)(OH_2)]^+$ (hereafter Pd^{II}_{eq}) reacts with *native* HSA, all possible binding sites are available for ligand uptake. The Trp-214 fluorescence quenching (static over the full range), reaction stoichiometry, and logK_a data (Figures 6a and 6b) indicate that

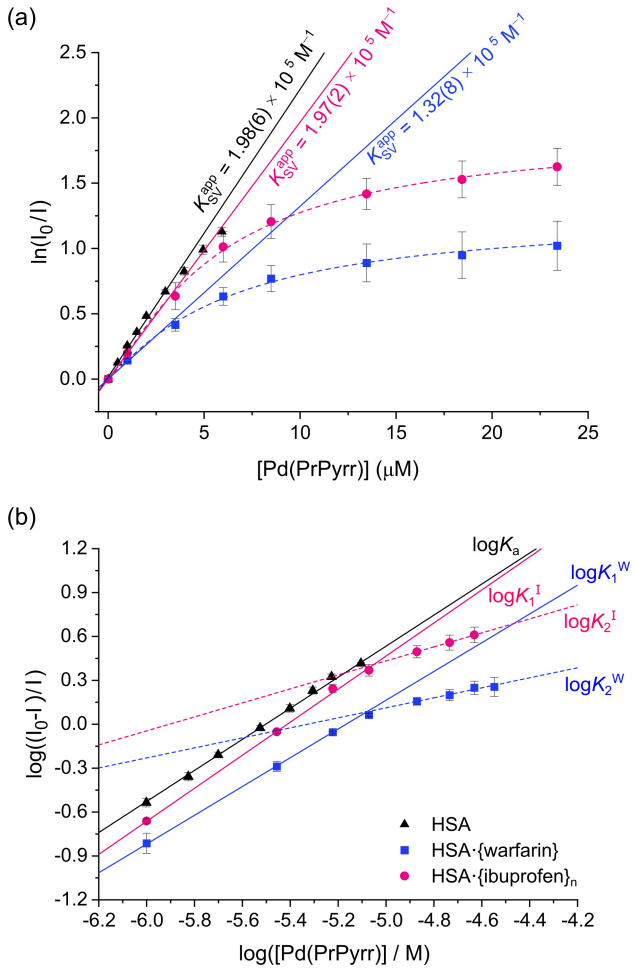

Figure 6. (a) Binding site determination for the reaction of Pd(PrPyrr) with HSA (5.0 μM protein, 50 mM KH_2PO_4, pH 7.50, 298 K) using a modified Stern-Volmer model (Equation S6), where $Pd^{II}_{eq} = [Pd(PrPyrr)] + [Pd(HPrPyrr)(OH_2)]^+$. For native HSA, Trp-214 is the fluorophore ($\lambda^{ex} = 280$ nm, $\lambda^{em} = 340$ nm). For drug-bound targets, 5.0 μM warfarin ($\lambda^{ex} = 320$ nm, $\lambda^{em} = 382$ nm) and 5.0-μM ibuprofen ($\lambda^{ex} = 228$ nm, $\lambda^{em} = 332$ nm) are the fluorophore probes. Warfarin binds specifically in Sudlow's site I (subdomain IIA), while ibuprofen is mainly bound in Sudlow's site II (subdomain IIIA). Native HSA exhibits static fluorescence (FL) quenching over the full concentration range ($K_{SV} = 3.60 \pm 0.2 \times 10^5$ M^{-1}). HSA·{warfarin} and HSA·{ibuprofen}$_n$ initially show static FL quenching, which switches to dynamic FL quenching when $[Pd^{II}_{eq}] > 5$ μM and the drug is displaced from the protein. The limiting values of ln(I_0/I) for HSA·{warfarin} and HSA·{ibuprofen}$_n$ were 1.27 ± 0.08 and 1.90 ± 0.06, respectively. (b) Determination of the affinity constants of Pd^{II}_{eq} for native HSA, HSA·{warfarin}, and HSA·{ibuprofen}$_n$ using Equation (1). The plot is linear for native HSA over the full concentration range (log$K_1 = 6.0 \pm 0.07$, $n = 1.1 \pm 0.01$). There are two steps for the reaction of Pd^{II}_{eq} with HSA·{warfarin} (log$K_1^W = 5.08 \pm 0.05$, $n_1 = 0.98 \pm 0.01$; log$K_2^W = 1.82 \pm 0.17$, $n_2 = 0.34 \pm 0.04$) and HSA·{ibuprofen}$_n$ (log$K_1^I = 6.11 \pm 0.13$, $n_1 = 1.13 \pm 0.02$; log $K_2^I = 2.82 \pm 0.06$, $n_2 = 0.48 \pm 0.01$).

a nominally 2:1 metal:protein complex, abbreviated HSA·{Pd^{II}-(X)}$_2$, where X represents the ligand combinations in Equation (2), is formed by simultaneous ligand uptake in a single step (log$K_1 = 6.00 \pm 0.07$, $n = 1.1 \pm 0.01$, 298 K). Titration of HSA·{warfarin} with Pd^{II}_{eq} while monitoring the fluorescence emission from warfarin ($\lambda^{ex} = 320$ nm, $\lambda^{em} = 382$ nm) reveals, firstly, that stepwise binding of the Pd^{II} chelate(s) occurs and, secondly, that warfarin is displaced from the protein when [

Research Article
doi.org/10.1002/ceur.202300012

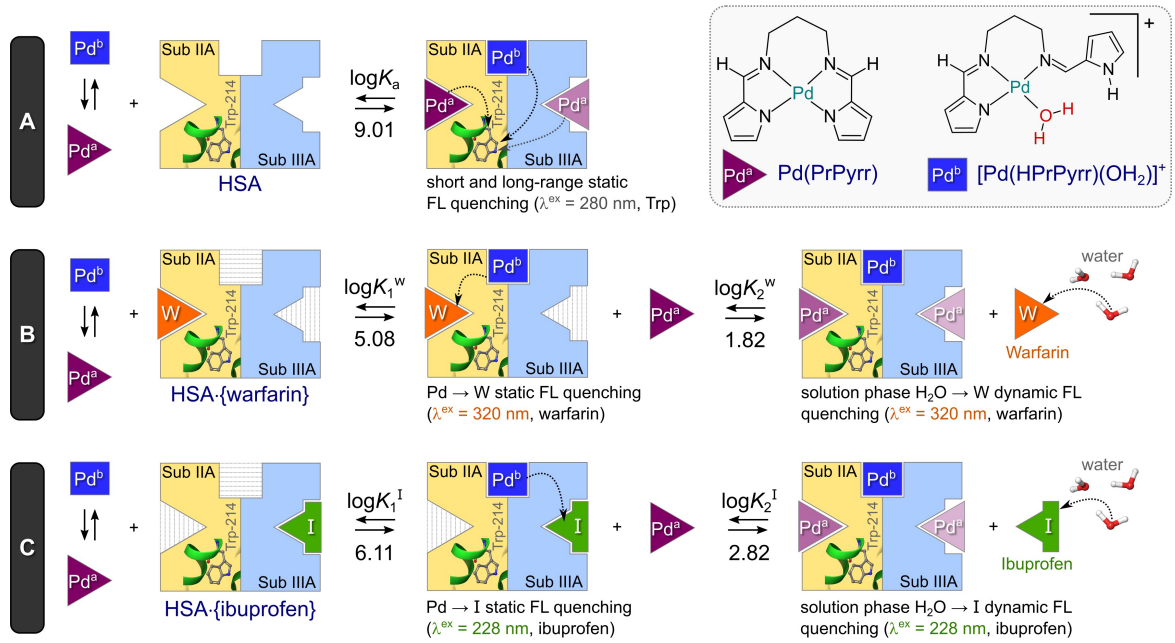

Figure 7. Proposed mechanism of interaction of a pH 7.5 equilibrium mixture of Pd(PrPyrr), comprising the tetradentate Pd^{II} chelate "Pd^a" and its tridentate aqua complex "Pd^b", with human serum albumin (HSA). The experimental affinity constants (298 K) and fluorophore excitation wavelengths are indicated; the diagram summarizes our best interpretation of the experimental data (Tables 1 and S8; Figures 5, 6 and S26) and in silico binding site specificity data. In **Part A**, the reaction of native HSA with the two Pd^{II} chelate species is shown. In addition to the main drug binding sites in subdomains IIA and IIIA of HSA (Sudlow's I and II, respectively), the existence of a third binding site unique to the Pd^{II} aqua complex is required to account for the spectroscopic and thermodynamic data. This binding site accommodates $[Pd(HPrPyrr)(OH_2)]^+$ and was found to be at the interfacial region between subunits IA-IIA/IIIA-IIA of the protein (Glide XP, Table S9). Pd(PrPyrr) preferentially binds in subdomain IIA, but also has some affinity for subdomain IIIA (indicated by different intensity purple triangles). All bound Pd^{II} chelates will contribute to efficient quenching of the emission from Trp-214 (dashed arrows). In **Part B**, HSA·{warfarin} is the reaction target. The binding pockets have diminished affinity due to allosteric effects (partial inhibition; dotted grey lines) from bound warfarin. This leads to step-wise binding of the Pd^{II} chelates with the affinity order $[Pd(HPrPyrr)(OH_2)]^+ > Pd(PrPyrr)$. Because the fluorescence titration monitors the emission from the drug probe directly (warfarin), its displacement and subsequent dynamic quenching by the solvent is readily detected. Pd(PrPyrr) fractionally occupies Sudlow's sites I and II in the product. **Part C** depicts the analogous reaction when the macromolecular target is HSA·{ibuprofen}$_n$. Notably, displacement of both warfarin and ibuprofen is mediated by Pd(PrPyrr) since $[Pd(HPrPyrr)(OH_2)]^+$ has a low affinity for these drug binding sites (Table S9) and Ni(PrPyrr) gives similar results (Figure S30; Tables S8 and S9). X-ray data will ultimately be required to confirm the proposed binding sites going forward.

$Pd^{II}_{eq}] > 5$ μM. The latter event is highlighted by the switch from static quenching of the emission from protein-bound warfarin to dynamic quenching of *free warfarin* in the solvent when $[Pd^{II}_{eq}] > 25$ μM (Figure 6a). The switch in the slope of the double-log plot of Figure 6b confirms stepwise uptake of the Pd^{II} chelate(s) by HSA·{warfarin}, which is characterized by independent affinity constants for each step ($\log K_1^W = 5.08 \pm 0.05$, $n_1 = 0.98 \pm 0.01$; $\log K_2^W = 1.82 \pm 0.17$, $n_2 = 0.34 \pm 0.04$) and an overall binding constant $\log \beta_2^W = 6.90$, which is 0.9 log units higher than $\log \beta_2$ measured for native HSA at 298 K.

The data from these experiments indicate simultaneous uptake of two Pd^{II} complexes at distinct sites located near Trp-214 in native HSA. When warfarin is bound to HSA in Sudlow's site I (subdomain IIA), only one Pd^{II} complex is initially bound-presumably at a site somewhat removed from the warfarin-binding pocket, but close enough to quench its fluorescence by a FRET-based mechanism. Since Sudlow's site II in subdomain IIIA is vacant at lower $[Pd^{II}_{eq}]$, ligand uptake could target this binding site, or a region close to it. However, we cannot rule out the binding of a Pd^{II} species at a unique location close to the warfarin binding site, for example, between subdomains IB and IIA (indomethacin secondary binding site), IA-IIA (fatty acid binding site, FA2), or even the secondary ibuprofen binding site (IIA-IIB).[92] Importantly, at a sufficiently high concentration of Pd^{II}_{eq}, warfarin is displaced from the protein by the uptake of a second partial equivalent ($n_2 < 1$) of the metal chelate. Evidently, at least one of the Pd^{II}_{eq} species, either $[Pd(HPrPyrr)(OH_2)]^+$ or Pd(PrPyrr), binds in Sudlow's site I (subdomain IIA), thereby directly competing with warfarin. From in silico docking data (see below), it seems likely that Pd(PrPyrr) targets Sudlow's site I and displaces warfarin.

What happens when we block binding of Pd^{II}_{eq} at Sudlow's site II in subdomain IIIA (and/or the protein's IIA-IIB binding site) using HSA·{ibuprofen}$_n$ as the target whilst monitoring the fluorescence from ibuprofen ($\lambda^{ex} = 228$ nm, $\lambda^{em} = 332$ nm)? From Figures 6a and 6b, the data mirror the observations for the warfarin adduct of the protein. Specifically, two-step binding of the Pd^{II} chelate(s) is evident due to well-separated $\log K_1$ and $\log K_2$ values ($\log K_1^I = 6.11 \pm 0.13$, $n_1 = 1.13 \pm 0.02$; $\log K_2^I = 2.82 \pm 0.06$, $n_2 = 0.48$ 0.01). Overall, $\log \beta_2^I = 8.93$ and the Pd^{II} chelates have a higher affinity for the ibuprofen adduct of the protein compared with the warfarin adduct. Interestingly, $\log K_1^I$ is almost identical to the binding of the Pd^{II} ligand to HSA, which could indicate Pd^{II} initially binds to HSA at an unpopulated site (likely Sudlow's site I), and as the ligand concentration increases, binding to a second site with lower affinity occurs.

Research Article
doi.org/10.1002/ceur.202300012

The first binding site will be within ~20 Å of the *bound ibuprofen fluorophores* to quench their emission by FRET. Crucially, displacement of ibuprofen from the protein occurs at high [Pd^{II}_{eq}]. The signature switch from static to dynamic quenching of the fluorophore when it is released into the bulk solvent is shown in Figure 6a. Interestingly, since $\log K^{I}_{2} > \log K^{W}_{2}$, ibuprofen is more readily displaced than warfarin from HSA.

One caveat is that M(PrPyrr) binding by HSA may induce conformational changes that trigger release of the blocking drug (fluorophore), even if the metal chelate does not target the drug's binding site directly (i.e., probe dissociation induced by allosteric effects). Although some uncertainty exists regarding the binding sites of the Pd^{II} chelates, the evidence points to Sudlow's sites I and II as being probable locations for ligand uptake. Such multi-site ligand binding is not uncommon—the organic drug diflunisal is known (X-ray data) to bind at multiple sites in HSA (specifically Sudlow's I and II, and between subdomains IIA and IIB).[92] Notably, ligands with multi-site binding to a promiscuous protein like HSA may fractionally populate two or more binding sites in a concerted uptake equilibrium (single step) to give an apparent reaction stoichiometry of $n \cong 1$ with a single log*K* value.

Our analysis of the dual-ligand binding mechanism for the reaction of native HSA with the Pd^{II} system above hinges on two species in solution [Equation (2)]. Dual-species uptake with subsequent Trp-214 fluorescence quenching is known for 3-hydroxyflavone (3-HF) with HSA.[93] Specifically, the two tautomers of 3-HF have similar, resolvable overlapping binding constants with HSA ($K_1 = 7.2\times10^5\ M^{-1}$ and $K_2 = 2.5\times10^5\ M^{-1}$) and bind in different binding sites (subdomains IIIA and IIA), affording unique Trp-214 quenching rate constants.[93] This is similar to what we observe for the two Pd^{II} species, Pd(PrPyrr) and $[Pd(HPrPyrr)(OH_2)]^+$, although we cannot resolve K_1 and K_2 for the binding of the two metal chelates due to their simultaneous uptake by the protein. Interestingly, the docking scores of the two Pd^{II} species are virtually the same (Table S9), mirroring the experimental data.

Mass spectroscopy confirms intact metal chelate uptake by HSA. We chose to analyse the complexes of HSA formed with the present metal chelates by ESI-MS to prove (i) that uptake of fully intact metal chelates occurs, (ii) multi-site binding is possible (consistent with $1 \leq n_{total} \leq 2$), and (iii) that the Pd^{II}(X) system behaves uniquely due to dual species uptake by the protein. From Figure S33 it is clear that the species HSA·{Ni(PrPyrr)}$_2$ was formed and dominant in the sample. In the case of Pt(PrPyrr), an entirely reasonable species distribution was evident: HSA (47%), HSA·{Pt(Pr(Pyrr)} (43%), and HSA·{Pt(Pr-(Pyrr)}$_2$ (10%). For the HSA-Pd^{II} system, the resolution of the data was not sufficient to distinguish between the chemical species bound, i.e., Pd(PrPyrr) and/or $[Pd(HPrPyrr)(OH_2)]^+$. However, a similar component distribution pattern to that seen for the Pt^{II} system was obtained, albeit with a lower fraction of the unbound protein: HSA (26%), HSA·{Pd(X)} (38%), and HSA·{Pd(X)}$_2$ (35%). Notably, the mass spectrum of the Pd^{II} system was unique in that satellite peaks appeared on the main bands at low m/z. Although minor in abundance, these peaks are likely due to covalent adducts formed when surface residues such as His[64] and Glu substitute Pd-bound water in $[Pd(HPrPyrr)(OH_2)]^+$. The kinetic inertness of Pt(PrPyrr) and Ni(PrPyrr) precludes the formation of such peaks.

Thermodynamics of metal chelate binding by HSA

The reactions of H_2PrPyrr and M(PrPyrr) with HSA follow a linear van't Hoff relationship; plots for triplicate measurements are given in Figure 8. Under non-standard conditions, the enthalpy change (ΔH), entropy change (ΔS), and Gibbs free energy change (ΔG), may be deduced from the temperature dependence of the affinity constants (K_a) using the van't Hoff and Gibbs-Helmholtz equations [Eqs. (S8)–(S10)]. Table 2 summarises the thermodynamic data for reaction of the compounds of interest with HSA in phosphate buffer at neutral pH. The reactions are all exergonic,[88] with ΔG ranging from $-20.3\ kJ\,mol^{-1}$ for H_2PrPyrr to $-33.1\ kJ\,mol^{-1}$ for Pd^{II}(X) at 298 K.

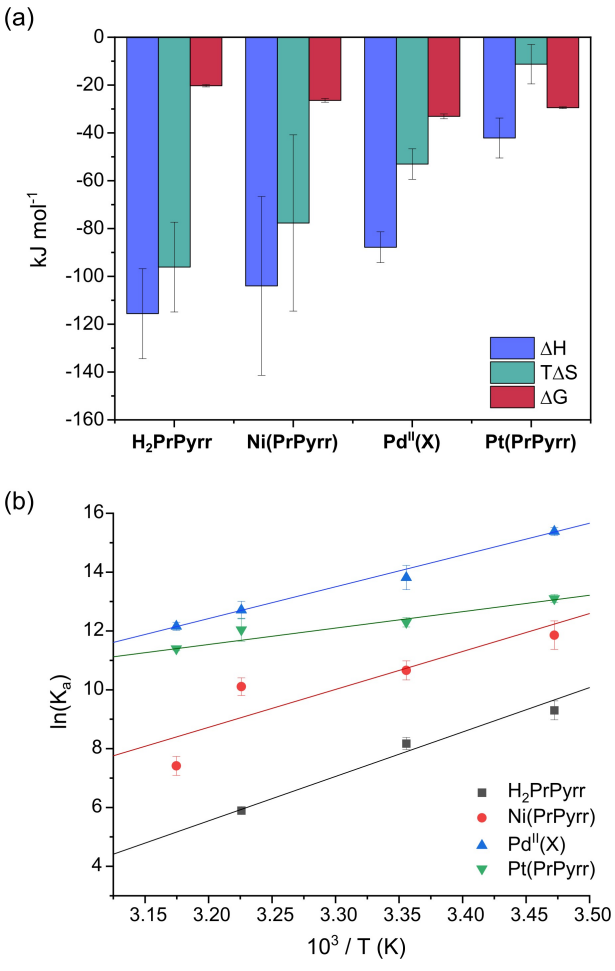

Figure 8. (a) Thermodynamic parameters governing the reactions of H_2PrPyrr and its d^8 Group 10 metal chelates with HSA ($T = 298$ K). Error bars are based on estimated uncertainties from the slope and intercepts of the least-squares fits of Equation S8 to the data. (b) Linear van't Hoff plots (Eq. S8) for the reactions of the compounds with HSA in 50 mM KH_2PO_4 buffer at pH 7.50. Error bars are estimated uncertainties derived from averaging triplicate measurements. Pearson's *r*-values for the fits were 0.99, 0.85, 1.00, and 0.99 for H_2PrPyrr, Ni(PrPyrr), Pd^{II}(K), and Pt(PrPyrr), respectively.

Research Article
doi.org/10.1002/ceur.202300012

Table 2. Thermodynamic parameters for the binding of H_2PrPyrr, Ni-(PrPyrr), Pd^{II}(X) and Pt(PrPyrr) by HSA in 50 mM KH_2PO_4 buffer at pH 7.50.

Compound	T [K]	ΔG [kJ mol^{-1}][a]	ΔH [kJ mol^{-1}][a]	ΔS [J K^{-1} mol^{-1}][a]
H_2PrPyrr	288	−22.3 (8)		
	298	−20.3 (5)	−116 (19)	−323 (96)
	310	−15.2 (3)		
Ni(PrPyrr)	288	−28.4 (1.2)		
	298	−26.4 (8)	−104 (37)	−261 (78)
	310	−26.1 (8)		
	315	−19.4 (8)		
Pd^{II}(X)[b]	288	−36.8 (3)		
	298	−33.1 (1.0)	−88 (6)	−178 (53)
	310	−30.4 (7)		
	315	−29.1 (3)		
Pt(PrPyrr)	288	−31.4 (3)		
	298	−29.5 (4)	−42 (8)	−38 (11)
	310	−28.8 (9)		
	315	−27.3 (2)		

[a] The estimated standard uncertainties of the least significant digits are given in parentheses. [b] X represents the ligand combinations shown in Equation (2).

As graphically portrayed in Figure 8a, the values of ΔH and $T\Delta S$ become increasingly *less negative* moving from the free ligand down the divalent Group 10 metal ions, increasing with the order 3d < 4d < 5d, while the values of ΔG display the reverse trend and become more negative going down the group. The switch in the order of ΔG evident for the Pt^{II} and Pd^{II} derivatives reflects the species distribution for the Pd^{II} system in Equation (2).

The spontaneity of metal chelate binding by HSA thus increases with increasing electron density within the complexes, which occurs naturally as the size of the metal ion and its polarizability (i.e., softness) increases.[94,95] The trend is driven by the reactions becoming less exothermic and more entropically favoured with the ΔH and $T\Delta S$ terms being of similar magnitude. Since London dispersion forces (LDF) of attraction in biomolecules significantly control the tertiary structure of the macromolecule,[96] and will increase in the order 3d < 4d < 5d[95] for this class of pyrrolide-imine metal chelates, Figure 8 suggests the reaction thermodynamics hinge on a significant LDF effect.

Regarding the ΔH values for the reactions, which are exothermic and range from −42 kJ mol^{-1} for Pt(PrPyrr) to −116 kJ mol^{-1} for H_2PrPyrr, Figure 8a highlights the significance of the enthalpy term and suggests that hydrogen bonding in the case of H_2PrPyrr accounts for its large negative values of ΔH and $T\Delta S$. Since the drug binding sites known as Sudlow's I and II (subdomains IIA and IIIA) in the protein are mostly hydrophobic,[45] the large negative $T\Delta S$ values for ligand binding recorded here imply enhanced conformational rigidity and minimal disruption of the protein's ordered water or backbone structure, commensurate with ligand uptake in one or more hydrophobic pockets, a deduction confirmed by our molecular docking simulations (see below).

The Gibbs-Helmholtz equation reveals the fundamentals of M(PrPyrr) binding by HSA. By using the Gibbs-Helmholtz equation (Eq. S10) with the experimental data (Table 2), the role played by the d^8 metal ion in determining the thermodynamics governing ligand uptake by HSA may be delineated (Figure 9). We have coined the term "*beads on a wire plot*" for this format of the Gibbs-Helmholtz equation as the points are free to move along the straight line and will cluster informatively within three of the four quadrants depending on the specific ligands and macromolecule being investigated for a spontaneous reaction. The plot is universal. For the present system, when $T\Delta S/\Delta G$ is plotted against $\Delta H/\Delta G$, the data fit the linear relationship in the upper right quadrant of the graph where $\Delta H < 0$, consistent with enthalpic control of the reaction. In this quadrant, spontaneity is assured as changes in $\Delta H/\Delta G$ are compensated for by commensurate changes in $T\Delta S/\Delta G$. Importantly, $T\Delta S/\Delta G$ and $\Delta H/\Delta G$ decrease together giving the order Pt(PrPyrr) < Pd^{II}(X) < Ni(PrPyrr), which follows the principal quantum number for the metal ion (5d < 4d < 3d). The trend indicates that the thermodynamics of metal chelate binding by HSA depends directly on increasing the electron density present in the complexes (i.e., LDF). The free ligand (H_2PrPyrr) has no metal centre so its binding to HSA hinges on both the π-electron density of the pyrrole-imine groups as well as the pyrrole N–H groups, which are excellent H-bond donors.[97,98]

The ligand binding thermodynamics here mirror data reported from microcalorimetry studies on the binding of drugs such as ibuprofen,[99] benzodiazepines,[100] and phenothiazines by HSA,[101] which have moderately negative ΔH (−50 to −75 kJ mol^{-1}) and ΔS values as well as sizeable K_{a1} values ~10^5 M^{-1}.[102] In the first association equilibrium, these drugs all bind in hydrophobic Sudlow's site II (subdomain IIIA) of HSA. Interestingly, a second ligand association may occur (dual-site binding, also in subdomain IIIA) with K_{a2} values ~10^3 M^{-1} and similarly negative ΔH and ΔS values.[102] Warfarin, which binds in Sudlows's site I (subdomain IIA),[91] has broadly comparable thermodynamics[102] ($logK_{a1} = 5.15$, $\Delta H = -49$ kJ mol^{-1}, $\Delta S =$

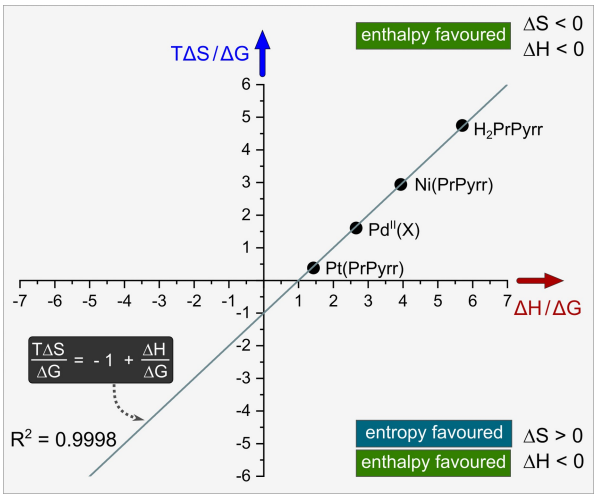

Figure 9. Plot of the Gibbs-Helmholtz relationship for the reaction of H_2PrPyrr, Ni(PrPyrr), Pd^{II}(X), and Pt(PrPyrr) with HSA at 298 K in 50 mM KH_2PO_4 buffer at pH 7.50. The straight line fit of the data gives $R^2 = 0.997$ with a slope of 1.001 ± 0.006 and intercept of −1 (fixed). For all reactions, $\Delta G < 0$. The plot highlights how the identity of the d^8 metal ion influences the reaction thermodynamics. (X represents the ligand combinations shown in Equation (2).)

Research Article
doi.org/10.1002/ceur.202300012

$-12\ J K^{-1} mol^{-1}$) to ibuprofen (Sudlow's site II, $logK_{a1} = 5.04$, $\Delta H = -67\ kJ mol^{-1}$, $\Delta S = -34\ J K^{-1} mol^{-1}$) and Ni(PrPyrr) ($logK_a = 4.92$, $\Delta H = -45\ kJ mol^{-1}$, $\Delta S = -57\ J K^{-1} mol^{-1}$), suggesting that assigning the specific binding site of the ligand ultimately requires additional structural or spectroscopic data.

Ligand-induced HSA secondary structure changes

Ligand binding minimally perturbs HSA. Since the far UV-region CD spectra of HSA (and other proteins) are sensitive to changes in the secondary (and tertiary) structure of the protein caused by ligand binding (i.e., perturbations of α-helices, β-sheets, hairpin turns and unordered coils),[103,104] CD spectroscopy (185–260 nm) was used to delineate how H_2PrPyrr and M(PrPyrr) impact the secondary structure of the protein (Figure 10). The CD spectrum of native HSA exhibits a double minimum (208 ± 1 nm and 222 ± 1 nm), reflecting a mainly α-helical structure.[105] The electronic transitions in this region are assigned to π-π* (208 nm minimum), n-π* (222 nm minimum), and π-π* (196 nm maximum) transitions of the amide groups of the peptide backbone.[105,106] From Figures 10a-10d, HSA binds the current ligands not only with high affinity (Table 1), but also with only minor changes in its secondary structure elements (the spectrum of native HSA is similar to the spectra in the presence of saturating ligand doses). Thus, the wavelengths of the band maxima and minima are largely unshifted, with only slight changes in intensity evident (most noticeably for the 196-nm band). The isodichroic points are quite difficult to locate, but those that are discernible appear to be somewhat sensitive to the identity of the bound ligand. In particular, there is some agreement between the wavelengths of the isodichroic points for HSA·{H_2PrPyrr} and HSA·{Pd^{II}(X)} as well as those for HSA·{Ni-(PrPyrr)} and HSA·{Pt(PrPyrr)}.

The CD data were analysed further (JASCO Spectra Manager™) to calculate the percentage composition of α-helical coils, β-sheets, turns, and unordered coils present for each HSA-ligand complex (Table S7). The dominant secondary structure domains are α-helices (~50%), and unordered coils (~31%), while β-sheet domains (8–19%) show the largest variation with the identity of the bound ligand. Interestingly, the secondary structure of HSA in solution differs from that of native HSA in the solid state[45] (68.5% α-helix, 0% β-sheet, 9.6% turns, and 21.9% unordered coils; PDB code 1BM0 analysed with BeStSel[107]). Our CD data are, however, consistent with solution state spectral decompositions reported by others,[108–110] and it is

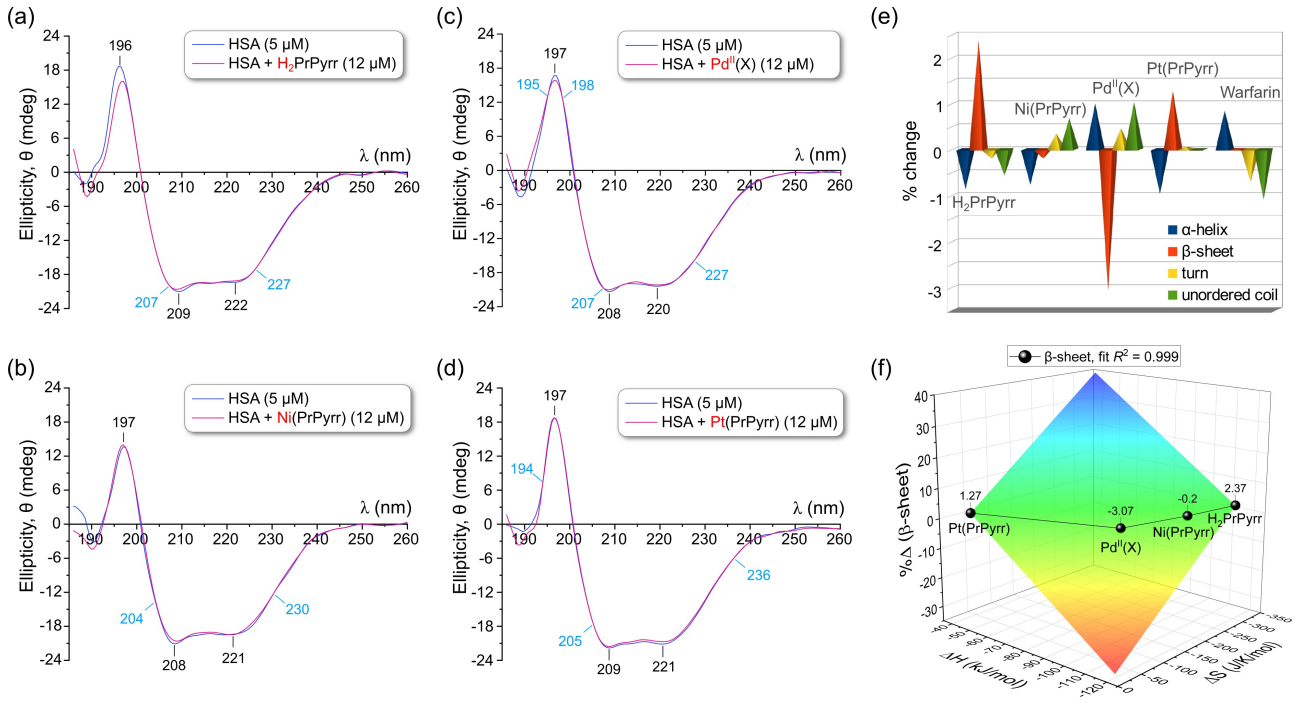

Figure 10. Plots of the far-UV CD spectra of native HSA and the protein incubated with saturating doses of (a) H_2PrPyrr, (b) Ni(PrPyrr), (c) Pd^{II}(X), and (d) Pt(PrPyrr) recorded at 298 K in 50 mM KH_2PO_4 buffer at pH 7.50. (For the Pd^{II} complex, X represents the ligand combinations of the equilibrium species depicted in Equation (2).) The spectra were smoothed using a Lowess function (0.07 span); unsmoothed spectra at ligand doses ranging from 4 μM to 12 μM are given in Supporting Information Figure S34. Band maxima and minima (black numerals) as well as isodichroic points (blue numerals) are indicated (in nm). (e) Graph of the percentage change in the protein secondary structure delineated by fitting the CD spectra in Parts (a)–(d). Data for warfarin were determined from the X-ray structures of the native (PDB code: 1BM0) and ligand-bound (PDB code: 2BXD) proteins using the program BeStSel. Although the protein is minimally perturbed by ligand uptake, the β-sheet content decreases by as much as 3% in the case of the complex formed with the Pd^{II} chelate. (f) Three-dimensional graph showing how the percentage change in the β-sheet content of the protein correlates with the experimentally determined values of ΔH and ΔS for the reaction of each compound with HSA ($T = 298$ K). The relationship, $\%\Delta(\beta\text{-sheet}) = 17.8(3) + 0.514(9) \times \Delta H - 0.136(2) \times \Delta S$, reflects the fact that ΔG for the reaction becomes more favourable (negative) as the β-sheet content of the protein decreases, which is dependent on the identity of the bound ligand and is matched by a commensurate *increase* in the α-helix content of the protein (see Supporting Information Figure S35). The correlation coefficient for the least-squares fit is exceptional considering the small sample size.

Research Article
doi.org/10.1002/ceur.202300012

understood that enhanced subdomain mobility and general thermal motion/disorder accounts for the decrease of α-helicity.[104,105]

HSA structural perturbations correlate with ligand binding thermodynamics. In Figure 10e, we have plotted the change in the secondary structure components of HSA as the percentage difference between the domain content for the native protein and that determined for the ligand-bound complex at saturation (Table S7). For the α-helix, turn, and coil regions of the structure, the ligand-induced perturbation falls within the range ±1.3%, which is comparable to the X-ray data for HSA bound to warfarin.[91] However, for the β-sheet domains, the ligand-induced perturbation is significantly greater with a range of ±3.1%. The complexes HSA·{H_2PrPyrr} and HSA·{Pd(PrPyrr)} exhibit the largest increase and decrease in β-sheet content, respectively.

Importantly, the ligand-induced changes in the protein secondary structure correlate with the thermodynamics of ligand binding measured independently by fluorescence spectroscopy. Thus, as shown in Figure 10f, the percentage change in the β-sheet composition, %Δ(β-sheet), is linearly co-dependent on the enthalpy and entropy changes for the reaction. Specifically, as ΔH and ΔS become more negative and positive, respectively, the β-sheet content *decreases* while the α-helix content *increases* (Figure S35). From the Gibbs-Helmholtz equation ($\Delta G = \Delta H - T\Delta S$), a more exergonic reaction (negative ΔG) reflects a decrease in β-sheet content. Ligand binding, which induces a modest increase in α-helicity, thus stabilizes the protein secondary structure,[111] in accord with the fact that α-helices are usually more stable thermodynamically than β-sheets.[112,113]

Intact metal chelates are bound by HSA

CD spectroscopy illuminates key ligand binding sites. Near-UV CD spectra provide a valuable fingerprint of protein tertiary structure perturbations, specifically those involving Trp (285–300 nm), Tyr (280 nm), and Phe (250–270 nm). Additionally, induced circular dichroism (ICD) spectra are informative when an optically inactive guest interacts with a protein and gains chirality from its chiral host.[106] Here, experimental CD spectra of the HSA-ligand complexes are included with an integrated interpretation of the data based on our Glide XP[114,115] molecular docking and TD-DFT simulations of the electronic structures of the protein-bound metal chelates. Figure 11 shows the near-UV and visible CD spectra of HSA recorded in native form and in the presence of identical saturating doses (12 μM) of H_2PrPyrr, Ni(PrPyrr), Pt(PrPyrr), and Pd^{II}(X), where X represents the ligands of Equation (2). Using difference spectroscopy, the ICD spectra were resolved for all ligands. The intensity of the ICD response followed the order $Pd^{II}(X) > Pt(PrPyrr) > Ni(PrPyrr) > H_2PrPyrr$, which is identical to the order of the affinity constants ($\log K_a$, Table 1) for the compounds.

Evidently, the stronger the HSA-ligand interaction, the greater the induced chirality in the formally achiral ligand. Importantly, the ICD spectra indicate that the complexes neither demetallate nor suffer imine hydrolysis or ligand dissociation when binding to HSA. Since ligand dissociation often accompanies HSA binding by simple metal complexes such *trans*-[$RuCl_4$(1*H*-indazole)$_2$]$^-$ (KP1019)[55] and cisplatin,[116] the present findings highlight the potential for fully reversible transport of the present and related compounds by HSA.

For HSA·{H_2PrPyrr} and HSA·{Ni(PrPyrr)}, the weaker ICD spectra of the ligands permit delineation of subtle changes in the fine structure CD bands of the protein host (Figure S36). Clear perturbation of the signal from Tyr (~277 nm) is evident in the difference spectrum for HSA·{H_2PrPyrr} (Figure 11a), consistent with this ligand and/or its protonated forms binding adjacent to one or more tyrosine residues, perhaps aided by H-bonding.[97] From our in silico docking data obtained with different grids (see below, Figure S37, Tables S10 and S11) there are several possible binding sites found within 10–27 Å of Trp-214 that can account for (i) FRET-based quenching of this fluorophore and (ii) location of the ligand within 4–10 Å of at least one Tyr residue. Interestingly, none of the binding sites are directly in the main drug-binding pockets of the protein (i.e., Sudlow's sites I and II). This evidently explains why blocking these sites with warfarin and ibuprofen neither inhibited the uptake of H_2PrPyrr (and/or its protonated forms) nor resulted in displacement of the probe drugs at higher ligand doses (Table S8, Figure S32).

For HSA·{Ni(PrPyrr)}, the near-UV CD signals from Phe (~269 nm), Tyr (~279 nm), and Trp-214 (~290 nm) showed significant perturbations (Figure 11b), commensurate with binding of the Ni^{II} chelate in one or more sites containing Phe and Tyr residues and within range of Trp-214 for FRET-based quenching (~1–3 nm in an isolated biomolecule).[117] From our Glide XP data, Ni(PrPyrr) favours binding in Sudlow's site I (Tables S9, S11) and possibly also Sudlow's site II. Medium-range dipole–dipole interactions between Ni(PrPyrr) and the closest Phe and Tyr residues within the binding pocket of Sudlow's site I (Table S10, Figure S36) are thus feasible given the spatial proximity of the chromophores (e.g., Tyr-150···Ni, 7.0 Å; Phe-149···Ni, 8.5 Å), accounting for the experimental near-UV CD data.

Regarding assignment of the near-UV and visible ICD spectrum of HSA·{Ni(PrPyrr)}, peaks with positive (300–340 nm; 375–430 nm) and negative ellipticity (457 and 477 nm) are observed (Figure 11b). Since unbound Ni(PrPyrr) is achiral (exact *Cs* symmetry), it has no CD spectrum. The electronic absorption spectrum of the protein-free Ni^{II} chelate is characterized by absorption maxima with $\varepsilon > 4\times10^3\ M^{-1}\,cm^{-1}$ at 313, 369, 388, 409, and 433 nm in pure acetonitrile (Figure S39). Considering the TD-DFT data for Ni(PrPyrr) (Table S12), these bands may be assigned to MLCT (metal-to-ligand charge transfer) transitions from filled MOs with mainly metal 3*d*-orbital character (and some ligand π character) to vacant MOs with mainly ligand π* character. (A broad, weaker band with $\varepsilon \sim 200\ M^{-1}\,cm^{-1}$ at ~523 nm encompassing one or more *d-d* transitions of the complex is also evident.) The MLCT absorption bands at 369 and 388 nm redshift by ~20–30 nm upon uptake of the Ni^{II} chelate by HSA, giving rise to the positive ICD bands at 404 and 421 nm. Similarly, those at 409 and 433 nm equate with the

Research Article
doi.org/10.1002/ceur.202300012

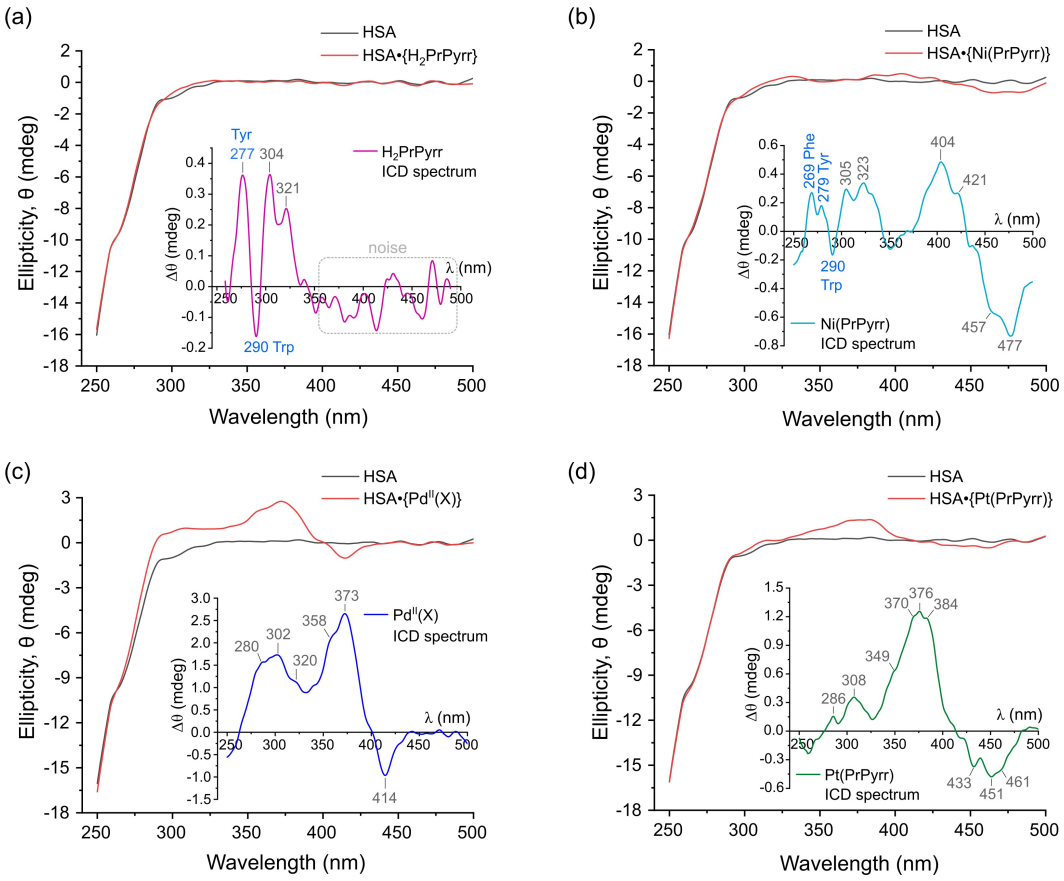

Figure 11. Plots of the near UV-visible CD spectra of native HSA (5 μM) and the protein incubated with a saturating dose (12 μM) of (a) H_2PrPyrr, (b) Ni(PrPyrr), (c) Pd^{II}(X), and (d) Pt(PrPyrr). The spectra were recorded at 298 K in 50 mM KH_2PO_4 buffer at pH 7.50 and smoothed using a relatively fine Lowess function (0.07 span). The graphical insets are plots of the difference spectra generated by subtraction of the spectrum of native HSA from that of the HSA-ligand complex; they represent the induced CD (ICD) spectrum of each achiral protein-bound ligand. (For the Pd^{II} complex, X represents the ligand combinations of the equilibrium species depicted in Equation (2)) Perturbations in the protein structure around Phe (250–270 nm), Tyr (~280 nm), and Trp (285–300 nm) residues may also be resolved in some difference spectra. Key maxima and minima are indicated (in nm). H_2PrPyrr has no visible absorption spectrum; undulations >350 nm are noise. Selected unsmoothed spectra are available in the Supporting Information (Figure S36). The CD spectra for all HSA·{ligand} complexes closely match the shoulder at ~262 nm of the native protein, suggesting the 17 disulphide bonds of the protein remain unchanged upon ligand uptake.

negative ICD bands at 457 and 477 nm (Figure S39). The fact that signals from Ni(PrPyrr) are discernible in the experimental CD spectrum of the protein complex, HSA·{Ni(PrPyrr)}, strikingly confirms that the intact Ni^{II} chelate is noncovalently bound within the protein. Significantly, TD-DFT simulations with the best-scoring pose for Ni(PrPyrr) docked within subdomain IIA of the protein (Table S9, Figure S40) support this conclusion by reproducing the main features of the experimental ICD spectrum.

The ICD spectrum recorded for HSA·{Pt(PrPyrr)} is akin to that of HSA·{Ni(PrPyrr)} and may be similarly assigned after taking into account the blue shift in the transition energies associated with the heavier metal ion. Indeed, the ICD spectra suggest that Pt(PrPyrr) targets the same binding site(s) as Ni(PrPyrr), consistent with our in silico docking data (Table S10).

The ICD spectrum of HSA·{Pd^{II}(X)} is the most intense of the series and shows features reminiscent of the above M(PrPyrr) chelates, specifically the peaks with positive ellipticity at 358 and 373 nm and the peak with negative ellipticity at 414 nm. One clear difference is the stronger set of positive ellipticity bands from 280–305 nm ($\Delta\theta \sim 1.7$ mdeg). These bands overlap the CD signals expected from perturbed Tyr and Trp residues; in the present system, they also reflect the interaction of HSA with the C_1-symmetry aqua complex, $[Pd(HPrPyrr)(OH_2)]^+$. We used Glide XP to dock both species depicted in Equation (2), i.e., Pd(PrPyrr) and $[Pd(HPrPyrr)(OH_2)]^+$, into HSA (PDB code: 1HA2) using a large 40^3 Å^3 grid centred on Trp-214 or the warfarin binding site as well as a similarly-constructed grid for the diazepam adduct of HSA (PDB code: 2BXF). The two best-scoring poses for the Pd^{II} chelates are located at sites in subdomain IIA of HSA (Tables S9–S11, Figure S41). Specifically, Pd(PrPyrr) favours the larger Sudlow's I site ($\Delta G_{dock} = -5.56$ kcal mol^{-1}) in a region directly adjacent to the warfarin binding site (Figure S42), while $[Pd(HPrPyrr)(OH_2)]^+$ binds towards the protein surface between two α-helical coils belonging to subunits IA and IIA ($\Delta G_{dock} = -5.53$ kcal mol^{-1}; Figure S41).

Research Article
doi.org/10.1002/ceur.202300012

TD-DFT simulations confirm intact metal chelate binding. Given the stoichiometry and fluorescence quenching data for the HSA-Pd^{II} system (Table 1), attempts to calculate the ICD spectrum of the system must include both Pd^{II} chelates. A hybrid QM:MM TD-DFT simulation (ONIOM[118] method, CAM–B3LYP[119]/SDD[120]/GD3BJ:[121] UFF[122]) was thus employed in which the two Pd^{II} chelates were assigned to the quantum mechanics (QM) layer of a model taken directly from the optimized Glide XP structure (Figure S41). Three side-chains belonging to residues closely interacting with Pd(PrPyrr) in Sudlow's site I (Arg-257, His-288, and Tyr-150) were added to the QM layer to calculate the most accurate CD spectrum (Figure S43). The remining atoms of the protein were simulated using molecular mechanics (UFF[122]). From Figure 12, the calculated CD spectrum of the system broadly matches the key features of the experimental ICD spectrum. Significantly, the analogous TD-DFT CD spectra for each Pd^{II} chelate independently bound to HSA poorly matched the experimental ICD spectrum (Figure S43), supporting our understanding of the HSA·{Pd^{II}(X)} system (i.e., dual chelate binding). One caveat is the remaining uncertainty concerning whether [Pd(PrPyrr)(OH$_2$)]$^+$ binds HSA non-covalently (as modelled) or covalently (e.g., via a surface residue such as His, Glu, or Cys substituting Pd-bound water). Although including noncovalently bound [Pd(PrPyrr)(OH$_2$)]$^+$ in the TD-DFT simulation was obligatory to match the positive ellipticity bands from 275 to 325 nm in the CD spectrum, only X-ray data will be definitive.

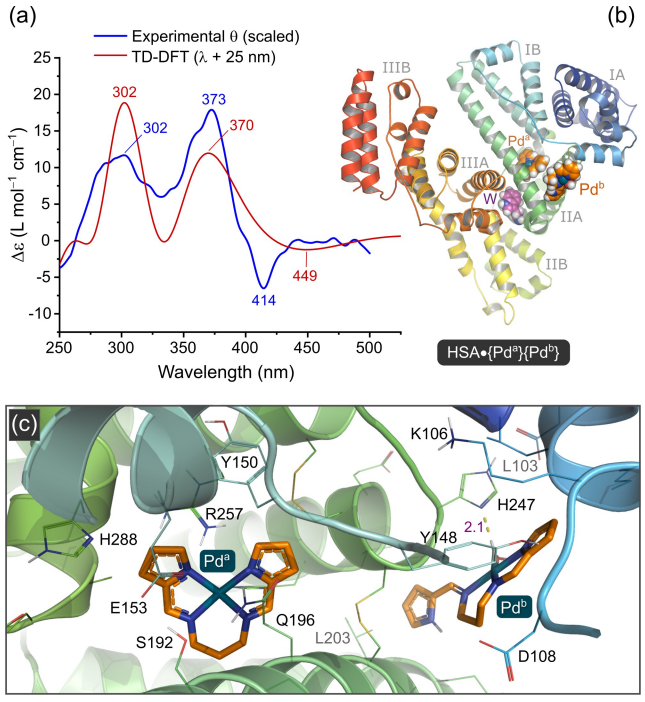

Figure 12. (a) Comparison of the experimental ICD spectrum (Δθ × 9 mdeg) recorded for HSA·{Pd^{II}(X)} at pH 7.5 (Figure 11c) and the CD spectrum calculated using hybrid QM:MM TD-DFT simulations (CAM–B3LYP/SDD/GD3BJ:UFF) for the top-scoring docked poses of Pd(PrPyrr), Pd^a, and [Pd(HPrPyrr)(OH$_2$)]$^+$, Pd^b, co-bound to HSA (PDB code: 1HA2). Both poses were required to get a reasonable match with the experimental data (Figure S43); a band width of 2500 cm^{-1} (hwhm) was used for the TD-DFT data. (b) Structural model used for the TD-DFT simulations showing the location of the two Pd^{II} chelates (orange C atoms, van der Waals radii) and Trp-214 (purple C atoms) in different regions of subdomain IIA (see also Figure S41). (c) View of the metal chelate binding sites containing the best poses of the two Pd^{II} complexes and their closest residues (1-letter codes). His-247 hydrogen bonds to the coordinated water molecule of [Pd(HPrPyrr)(OH$_2$)]$^+$ (O–H···N, 2.08 Å, dashed yellow cylinder). Only polar hydrogen atoms are shown.

Macromolecular simulations reflect multi-site ligand binding

Docking studies (Glide XP) were used to predict possible HSA binding sites for the present ligands along with control compounds (warfarin, diazepam, ibuprofen). Since rigid X-ray structures of proteins are used as the hosts for flexible ligand docking, the method offers approximate insights on target binding. Notably, docking scores do not correlate quantitatively with experimental thermodynamic data (ΔG values)[123,124] because the in silico experiment does not try to emulate a physical reaction between the macromolecule and incoming ligand in solution. Thus, only qualitative parallels are drawn between the thermodynamic data (Tables 1, 2, and S8) and docking scores of Tables S9 and S11, with a focus on simulations enhancing our understanding of the experimental facts. The key trends are enumerated below:

1. The existence of multiple binding sites within HSA for the current ligand set is predicted from the narrow range of docking scores (ΔG_{dock} ~ −3 to −7 kcal mol^{-1}) and repeatedly favoured binding locations (~7 in total including Sudlow's I and II), consistent with X-ray data for diverse drug and ligand types bound by HSA.[92]
2. The binding site locations were all within 5–20 Å of Trp-214, accounting for facile quenching of its emission by the ligands (Table 1). Furthermore, all were within 3.5–15 Å of tyrosine and/or phenylalanine residues (Table S10), affording observable CD signal perturbations between 250 and 295 nm for at least two HSA-ligand complexes (H_2PrPyrr and Ni(PrPyrr), Figure 11).
3. Warfarin bound within HSA (subdomain IIA), generally *enhances* the docking scores for ligand uptake when forming a multi-ligand complex (Table S9). Thus, ΔG_{dock} improves from −5.17 to −6.00 kcal mol^{-1} when Ni(PrPyrr) co-binds with warfarin (Figure S38) due to enhanced lipophilic van der Waals and electrostatic energy terms. In contrast, the docking score worsens from −5.56 to −4.01 kcal mol^{-1} for Pd(PrPyrr) when warfarin is co-bound in Sudlow's site I due to van der Waals repulsion between the metal chelate and the probe (Figure S42). These trends qualitatively mirror the experimental logK_a data for several ligands (Table S8).
4. Ibuprofen bound within Sudlow's site II (subdomains IIIA and IIA-IIB) decreases the docking scores for the ligands with HSA, a trend mirrored by the reaction thermodynamics (e.g., Ni(PrPyrr) and Pd^{II}(X) binding to HSA, Table S8). Although these ligands do not compete with ibuprofen for the same binding sites in the docking experiment (Table S9), ibuprofen seemingly redirects their uptake to less-favourable binding sites relative to those in native HSA. In reality, Pd^{II}(X) and Ni(PrPyrr) easily displace ibuprofen from HSA (Figures 6

Research Article
doi.org/10.1002/ceur.202300012

and S30), suggesting that these ligands can bind in subdomain IIIA (Table S11) or that the release of ibuprofen is triggered by allosteric effects when the ligands bind at the alternative locations.

Finally, the grid chosen for the docking simulation affects the docking-score order and in silico site specificity of the ligands for HSA (Tables S9 and S11). This limitation is well known with the use of a rigid receptor grid, as done here, considered best for some metalloproteins.[125] For this reason, and because there is no other way to guide the grid choice for novel ligands when X-ray data are absent, we have mainly used the data generated with a rigid receptor grid (Table S9) as opposed to that obtained with a soft receptor and ligand potential (Table S11). The results obtained with the softer potential may, however, be equally valid.

Conclusion

The interaction of H_2PrPyrr and its Ni^{II}, Pd^{II}, and Pt^{II} chelates with human serum albumin (HSA) was investigated by complementary spectroscopic techniques to understand how the identity of the d^8 metal ion affects ligand uptake by the protein. All ligands quenched the intrinsic Trp-214 fluorescence of HSA via a static quenching mechanism. The Stern-Volmer quenching constants (K_{SV}) and affinity constants (K_a) followed the order: Pd(PrPyrr) $\gg$ Pt(PrPyrr) $>$ Ni(PrPyrr) $>$ H_2PrPyrr. The notably higher affinity of Pd(PrPyrr) for HSA coupled with a reaction stoichiometry, *n*, *significantly exceeding* 1 : 1 (ligand:HSA) reflects simultaneous uptake of two Pd^{II} species from an equilibrium mixture comprising Pd(PrPyrr) and $[Pd(HPrPyrr)(OH_2)]^+$, the latter structure being related to the crystallographically-characterized chlorido complex, PdCl(HPrPyrr). Significantly, ESI-MS data directly confirmed formation of HSA·{ligand}$_n$ species with $n \geq 1$ for the M(PrPyrr) chelates. The present ligands bind to HSA with *negative* ΔH, ΔG and ΔS values, reflecting a spontaneous enthalpy-driven process governed by van der Waals (London dispersion) forces as well as H-bonding (for H_2PrPyrr). $T\Delta S/\Delta G$ and $\Delta H/\Delta G$ together become increasingly positive, following the order Pt(PrPyrr) $<$ Pd^{II}(X) $<$ Ni(PrPyrr) $<$ H_2PrPyrr, thereby inversely tracking the Group 10 metal ionic radii and polarizability order (5d $>$ 4d $>$ 3d). *In silico* data support the notion (gleaned from spectroscopy) that each ligand has more than one binding site in HSA and that ligand uptake minimally perturbs the protein's secondary structure. Finally, the induced CD spectra recorded for the metal chelates bound to HSA strikingly confirm uptake of the intact complexes without imine group hydrolysis or demetallation.

Experimental Section

Crystallographic data

Deposition Numbers 2207667 and 2207668 contain the supplementary crystallographic data for this paper. These data are provided free of charge by the joint Cambridge Crystallographic Data Centre and Fachinformationszentrum Karlsruhe Access Structures service. Full experimental details, computational methods, and characterization data are given in the Supporting Information.

Acknowledgements

This work is based on research supported by the South African Research Chairs Initiative of the Department of Science and Innovation (DSI) and National Research Foundation (NRF) of South Africa (Grant No 64799, OQM). The authors thank WITS University and the NRF for funding to purchase a JASCO J-1500 MCD spectrometer (Grant No 116177, OQM) and a dual-wavelength Bruker D8 Venture X-ray diffractometer (Grant No 129920, OQM). We also thank the Centre for High Performance Computing (Project CHEM1065, CHPC, Cape Town) for both the CPU time and resources needed for the DFT simulations.

Conflict of Interests

The authors declare no conflict of interest.

Data Availability Statement

The data that support the findings of this study are openly available in ChemRxiv at https://doi.org/10.26434/chemrxiv-2022-8v4x2-v2, reference number 9022023.

Keywords: albumin · DFT simulations · ligand binding · metal chelate · Schiff base

[1] R. U. Braun, K. Zeitler, T. J. J. Müller, *Org. Lett.* **2001**, *3*, 3297–3300.
[2] C. E. Hewton, M. C. Kimber, D. K. Taylor, *Tetrahedron Lett.* **2002**, *43*, 3199–3201.
[3] M. P. Akerman, V. A. Chiazzari, *J. Mol. Struct.* **2014**, *1058*, 22–30.
[4] X. Ren, B. D. Alleyne, P. I. Djurovich, C. Adachi, I. Tsyba, R. Bau, M. E. Thompson, *Inorg. Chem.* **2004**, *43*, 1697–1707.
[5] Y. Wang, T. Liang, J. Yao, T. Zhai, H. Fu, *Acta Crystallogr. Sect. E* **2008**, *64*, o629–o629.
[6] P. G. Sim, E. Sinn, *Inorg. Chem.* **1978**, *17*, 1288–1290.
[7] K. Hüttinger, C. Förster, T. Bund, D. Hinderberger, K. Heinze, *Inorg. Chem.* **2012**, *51*, 4180–4192.
[8] M. A. Rhine, A. V. Rodrigues, R. J. B. Urbauer, J. L. Urbauer, T. L. Stemmler, T. C. Harrop, *J. Am. Chem. Soc.* **2014**, *136*, 12560–12563.
[9] M. R. Walter, S. P. Dzul, A. V. Rodrigues, T. L. Stemmler, J. Telser, J. Conradie, A. Ghosh, T. C. Harrop, *J. Am. Chem. Soc.* **2016**, *138*, 12459–12471.
[10] D. Bandyopadhyay, M. Layek, M. Fleck, R. Saha, C. Rizzoli, *Inorg. Chim. Acta* **2017**, *461*, 174–182.
[11] S. A. Carabineiro, L. C. Silva, P. T. Gomes, L. C. J. Pereira, L. F. Veiros, S. I. Pascu, M. T. Duarte, S. Namorado, R. T. Henriques, *Inorg. Chem.* **2007**, *46*, 6880–6890.
[12] H. Brunner, B. Nuber, T. Tracht, *Tetrahedron: Asymmetry* **1998**, *9*, 3763–3771.
[13] H. Brunner, A. Köllnberger, M. Zabel, *Polyhedron* **2003**, *22*, 2639–2646.
[14] S. Basu, I. Pal, R. J. Butcher, G. Rosair, S. Bhattacharya, *J. Chem. Sci.* **2005**, *117*, 167–173.
[15] Y. Haketa, M. Miyasue, Y. Kobayashi, R. Sato, Y. Shigeta, N. Yasuda, N. Tamai, H. Maeda, *J. Am. Chem. Soc.* **2020**, *142*, 16420–16428.
[16] P. Paul, M. G. Richmond, S. Bhattacharya, *J. Organomet. Chem.* **2014**, *751*, 760–768.
[17] H. Brunner, A. Köllnberger, M. Zabel, *Polyhedron* **2003**, *22*, 2639–2646.

Research Article
doi.org/10.1002/ceur.202300012

[18] C. H. Wei, J. R. Einstein, *Acta Crystallogr. Sect. B* **1972**, *28*, 2591–2598.
[19] Y. Wang, H. Fu, F. Shen, X. Sheng, A. Peng, Z. Gu, H. Ma, J. S. Ma, J. Yao, *Inorg. Chem.* **2007**, *46*, 3548–3556.
[20] S. Bhikraj, O. Q. Munro, M. P. Akerman, *Polyhedron* **2017**, *124*, 22–29.
[21] J. S. Hart, G. S. Nichol, J. B. Love, *Dalton Trans.* **2012**, *41*, 5785–5788.
[22] H. Liang, J. Liu, X. Li, Y. Li, *Polyhedron* **2004**, *23*, 1619–1627.
[23] C. N. Iverson, C. A. G. Carter, R. T. Baker, J. D. Scollard, J. A. Labinger, J. E. Bercaw, *J. Am. Chem. Soc.* **2003**, *125*, 12674–12675.
[24] X.-F. Shan, D.-H. Wang, C.-H. Tung, L.-Z. Wu, *Tetrahedron* **2008**, *64*, 5577–5582.
[25] Y. Kim, J. Lee, Y.-H. Son, S.-U. Choi, M. Alam, S. Park, *J. Inorg. Biochem.* **2020**, *205*, 111015.
[26] C. H. Wei, *Inorg. Chem.* **1972**, *11*, 2315–2321.
[27] N. A. Bailey, A. Barrass, D. E. Fenton, M. S. L. Gonzalez, R. Moody, C. O. R. de Barbarin, *J. Chem. Soc. Dalton Trans.* **1984**, 2741–2746.
[28] F. Z. C. Fellah, J.-P. Costes, F. Dahan, C. Duhayon, G. Novitchi, J.-P. Tuchagues, L. Vendier, *Inorg. Chem.* **2008**, *47*, 6444–6451.
[29] Y. Hu, Q. Li, H. Li, Q. Guo, Y. Lu, Z. Li, *Dalton Trans.* **2010**, *39*, 11344–11352.
[30] H. Adams, M. R. J. Elsegood, D. E. Fenton, S. L. Heath, S. J. Ryan, *J. Chem. Soc. Dalton Trans.* **1999**, 2031–2038.
[31] K. J. Akerman, A. M. Fagenson, V. Cyril, M. Taylor, M. T. Muller, M. P. Akerman, O. Q. Munro, *J. Am. Chem. Soc.* **2014**, *136*, 5670–5682.
[32] V. Bhardwaj, D. Gumber, V. Abbot, S. Dhiman, P. Sharma, *RSC Adv.* **2015**, *5*, 15233–15266.
[33] R. N. Brogden, R. C. Heel, T. M. Speight, G. S. Avery, *Drugs* **1978**, *15*, 429–450.
[34] M. Atkins, C. A. Jones, P. Kirkpatrick, *Nat. Rev. Drug Discovery* **2006**, *5*, 279–280.
[35] H. D. Langtry, J. A. Balfour, *Drugs* **1998**, *55*, 563–584.
[36] S. Hannah, V. M. Lynch, N. Gerasimchuk, D. Magda, J. L. Sessler, *Org. Lett.* **2001**, *3*, 3911–3914.
[37] J. L. Sessler, T. D. Mody, G. W. Hemmi, V. Lynch, *Inorg. Chem.* **1993**, *32*, 3175–3187.
[38] W.-H. Wei, Z. Wang, T. Mizuno, C. Cortez, L. Fu, M. Sirisawad, L. Naumovski, D. Magda, J. L. Sessler, *Dalton Trans.* **2006**, 1934–1942.
[39] H. Patel, R. Mick, J. Finlay, T. C. Zhu, E. Rickter, K. A. Cengel, S. B. Malkowicz, S. M. Hahn, T. M. Busch, *Clin. Cancer Res.* **2008**, *14*, 4869–4876.
[40] C. Preihs, J. F. Arambula, D. Magda, H. Jeong, D. Yoo, J. Cheon, Z. H. Siddik, J. L. Sessler, *Inorg. Chem.* **2013**, *52*, 12184–12192.
[41] R. Gupta, C. Rodrigues Felix, M. P. Akerman, K. J. Akerman, C. A. Slabber, W. Wang, J. Adams, L. N. Shaw, Y.-C. Tse-Dinh, O. Q. Munro, K. H. Rohde, *Antimicrob. Agents Chemother.* **2018**, *62*, e01696–17.
[42] M. P. Akerman, O. Q. Munro, M. Mongane, J. A. van Staden, W. I. D. Rae, C. J. Bester, B. Marjanovic-Painter, Z. Szucs, J. R. Zeevaart, *J. Labelled Compd. Radiopharm.* **2013**, *56*, 530–535.
[43] S. Curry, *Drug Metab. Pharmacokinet.* **2009**, *24*, 342–357.
[44] G. J. Quinlan, G. S. Martin, T. W. Evans, *Hepatology* **2005**, *41*, 1211–1219.
[45] X. M. He, D. C. Carter, *Nature* **1992**, *358*, 209–215.
[46] P. A. Zunszain, J. Ghuman, T. Komatsu, E. Tsuchida, S. Curry, *BMC Struct. Biol.* **2003**, *3*, 6.
[47] G. Rabbani, S. N. Ahn, *Int. J. Biol. Macromol.* **2019**, *123*, 979–990.
[48] G. Sudlow, D. J. Birkett, D. N. Wade, *Mol. Pharmacol.* **1976**, *12*, 1052–1061.
[49] G. Sudlow, D. J. Birkett, D. N. Wade, *Mol. Pharmacol.* **1975**, *11*, 824–832.
[50] V. Tuan Giam Chuang, U. Kragh-Hansen, M. Otagiri, *Pharm. Res.* **2002**, *19*, 569–577.
[51] M. Fasano, S. Curry, E. Terreno, M. Galliano, G. Fanali, P. Narciso, S. Notari, P. Ascenzi, *IUBMB Life* **2005**, *57*, 787–796.
[52] O. Dömötör, T. Pivarcsik, J. P. Mészáros, I. Szatmári, F. Fülöp, É. A. Enyedy, *Dalton Trans.* **2021**, *50*, 11918–11930.
[53] É. A. Enyedy, J. P. Mészáros, O. Dömötör, C. M. Hackl, A. Roller, B. K. Keppler, W. Kandioller, *J. Inorg. Biochem.* **2015**, *152*, 93–103.
[54] O. Dömötör, É. A. Enyedy, *JBIC* **2019**, *24*, 703–719.
[55] A. Bijelic, S. Theiner, B. K. Keppler, A. Rompel, *J. Med. Chem.* **2016**, *59*, 5894–5903.
[56] L. Messori, A. Merlino, *Dalton Trans.* **2014**, *43*, 6128–6131.
[57] A. Casini, C. Temperini, C. Gabbiani, C. T. Supuran, L. Messori, *ChemMedChem* **2010**, *5*, 1989–1994.
[58] G. Ferraro, M. Paolillo, G. Sciortino, E. Garribba, A. Merlino, *Inorg. Chem.* **2022**, *61*, 16458–16467.
[59] F. Wang, J. Bella, J. A. Parkinson, P. J. Sadler, *JBIC* **2005**, *10*, 147–155.
[60] D. Stanic-Vucinic, S. Nikolic, K. Vlajic, M. Radomirovic, J. Mihailovic, T. Cirkovic Velickovic, S. Grguric-Sipka, *JBIC* **2020**, *25*, 253–265.
[61] L. Messori, F. G. Vilchez, R. Vilaplana, F. Piccioli, E. Alessio, B. Keppler, *Met.-Based Drugs* **2000**, *7*, 335–342.
[62] A. Casini, C. Gabbiani, E. Michelucci, G. Pieraccini, G. Moneti, P. J. Dyson, L. Messori, *JBIC* **2009**, *14*, 761–770.
[63] A. Casini, G. Mastrobuoni, C. Temperini, C. Gabbiani, S. Francese, G. Moneti, C. T. Supuran, A. Scozzafava, L. Messori, *Chem. Commun.* **2006**, 156–158.
[64] G. Marcon, L. Messori, P. Orioli, M. A. Cinellu, G. Minghetti, *Eur. J. Biochem.* **2003**, *270*, 4655–4661.
[65] Y.-C. Lo, T.-P. Ko, W.-C. Su, T.-L. Su, A. H.-J. Wang, *J. Inorg. Biochem.* **2009**, *103*, 1082–1092.
[66] O. Mazuryk, K. Magiera, B. Rys, F. Suzenet, C. Kieda, M. Brindell, *JBIC* **2014**, *19*, 1305–1316.
[67] A. Wragg, M. R. Gill, L. McKenzie, C. Glover, R. Mowll, J. A. Weinstein, X. Su, C. Smythe, J. A. Thomas, *Chem. Eur. J.* **2015**, *21*, 11865–11871.
[68] B. Sun, M. K. Sundaraneedi, H. M. Southam, R. K. Poole, I. F. Musgrave, F. Richard Keene, J. Grant Collins, *Dalton Trans.* **2019**, *48*, 14505–14515.
[69] N. Biswas, S. Khanra, A. Sarkar, S. Bhattacharjee, D. P. Mandal, A. Chaudhuri, S. Chakraborty, C. R. Choudhury, *J. Coord. Chem.* **2018**, *71*, 2740–2766.
[70] X.-F. Shan, D.-H. Wang, C.-H. Tung, L.-Z. Wu, *Tetrahedron* **2008**, *64*, 5577–5582.
[71] A. Bacchi, M. Carcelli, L. Gabba, S. Ianelli, P. Pelagatti, G. Pelizzi, D. Rogolino, *Inorg. Chim. Acta* **2003**, *342*, 229–235.
[72] T. Imamura, T. Tanaka, M. Fujimoto, *Inorg. Chem.* **1985**, *24*, 1038–1041.
[73] L. Pinard, J. Mijoin, P. Ayrault, C. Canaff, P. Magnoux, *Appl. Catal. B* **2004**, *51*, 1–8.
[74] A. J. McNeece, M.-C. Chang, A. S. Filatov, J. S. Anderson, *Inorg. Chem.* **2018**, *57*, 7044–7050.
[75] C. R. Groom, I. J. Bruno, M. P. Lightfoot, S. C. Ward, *Acta Crystallogr. Sect. B* **2016**, *72*, 171–179.
[76] O. K. Abou-Zied, O. I. K. Al-Shihi, *J. Am. Chem. Soc.* **2008**, *130*, 10793–10801.
[77] P. R. Callis, *J. Mol. Struct.* **2014**, *1077*, 14–21.
[78] Y. Yue, J. Liu, M. Yao, X. Yao, J. Fan, H. Ji, *Spectrochim. Acta Part A* **2012**, *96*, 316–323.
[79] P. R. Callis, *J. Mol. Struct.* **2014**, *1077*, 22–29.
[80] A. Divsalar, M. J. Bagheri, A. A. Saboury, H. Mansoori-Torshizi, M. Amani, *J. Phys. Chem. B* **2009**, *113*, 14035–14042.
[81] S. Goutelle, M. Maurin, F. Rougier, X. Barbaut, L. Bourguignon, M. Ducher, P. Maire, *Fundam. Clin. Pharmacol.* **2008**, *22*, 633–648.
[82] J. T. Vivian, P. R. Callis, *Biophys. J.* **2001**, *80*, 2093–2109.
[83] J. R. Lakowicz, *Principles of Fluorescence Spectroscopy*, Springer US, Boston MA, **2006**.
[84] Y.-J. Hu, Y. Liu, X.-H. Xiao, *Biomacromolecules* **2009**, *10*, 517–521.
[85] G. G. Ariga, P. N. Naik, S. A. Chimatadar, S. T. Nandibewoor, *J. Mol. Struct.* **2017**, *1137*, 485–494.
[86] X. Sun, S. Bi, J. Wu, R. Zhao, D. Shao, Z. Song, *J. Biomol. Struct. Dyn.* **2020**, *38*, 934–942.
[87] S. Soares, N. Mateus, V. de Freitas, *J. Agric. Food Chem.* **2007**, *55*, 6726–6735.
[88] P. D. Ross, S. Subramanian, *Biochemistry* **1981**, *20*, 3096–3102.
[89] X. Li, S. Wang, *New J. Chem.* **2015**, *39*, 386–395.
[90] P. D. Ross, S. Subramanian, *Biochemistry* **1981**, *20*, 3096–3102.
[91] I. Petitpas, A. A. Bhattacharya, S. Twine, M. East, S. Curry, *J. Biol. Chem.* **2001**, *276*, 22804–22809.
[92] J. Ghuman, P. A. Zunszain, I. Petitpas, A. A. Bhattacharya, M. Otagiri, S. Curry, *J. Mol. Biol.* **2005**, *353*, 38–52.
[93] A. Sytnik, I. Litvinyuk, *Proc. Natl. Acad. Sci. USA* **1996**, *93*, 12959–12963.
[94] P. W. Ayers, *Faraday Discuss.* **2006**, *135*, 161–190.
[95] R. G. Pearson, *J. Chem. Educ.* **1968**, *45*, 643.
[96] M. Kolář, T. Kubař, P. Hobza, *J. Phys. Chem. B* **2011**, *115*, 8038–8046.
[97] O. Q. Munro, G. L. Camp, *Acta Crystallogr. Sect. C* **2003**, *59*, o672–o675.
[98] O. Q. Munro, S. D. Joubert, C. D. Grimmer, *Chem. Eur. J.* **2006**, *12*, 7987–7999.
[99] H. Aki, M. Goto, M. Yamamoto, *Thermochim. Acta* **1995**, *251*, 379–388.
[100] R. E. Olson, D. D. Christ in *Annu. Rep. Med. Chem.* (Ed.: J. A. Bristol), Academic Press, **1996**, pp. 327–336.
[101] H. Aki, M. Yamamoto, *J. Pharm. Pharmacol.* **1989**, *41*, 674–679.
[102] H. Aki, M. Yamamoto, *J. Pharm. Sci.* **1994**, *83*, 1712–1716.
[103] N. J. Greenfield, *Nat. Protoc.* **2006**, *1*, 2876–2890.
[104] P. Alam, S. K. Chaturvedi, T. Anwar, M. K. Siddiqi, M. R. Ajmal, G. Badr, M. H. Mahmoud, R. Hasan Khan, *J. Lumin.* **2015**, *164*, 123–130.

Research Article
doi.org/10.1002/ceur.202300012

[105] N. Sreerama, R. W. Woody in *Methods Enzymol.*, Academic Press, **2004**, pp. 318–351.
[106] S. M. Kelly, T. J. Jess, N. C. Price, *Biochim. Biophys. Acta BBA-Proteins Proteomics* **2005**, *1751*, 119–139.
[107] A. Micsonai, F. Wien, É. Bulyáki, J. Kun, É. Moussong, Y.-H. Lee, Y. Goto, M. Réfrégiers, J. Kardos, *Nucleic Acids Res.* **2018**, *46*, W315–W322.
[108] F. Mohammadi, A.-K. Bordbar, A. Divsalar, K. Mohammadi, A. A. Saboury, *Protein J.* **2009**, *28*, 189–196.
[109] H. A. Tajmir-Riahi, C. N. N'soukpoé-Kossi, D. Joly, *Spectroscopy* **2009**, *23*, 81–101.
[110] O. Duman, S. Tunç, B. Kancı Bozoğlan, *J. Fluoresc.* **2013**, *23*, 659–669.
[111] G. Abrusán, J. A. Marsh, *PLoS Comput. Biol.* **2016**, *12*, e1005242.
[112] A.-S. Yang, B. Honig, *J. Mol. Biol.* **1995**, *252*, 366–376.
[113] A.-S. Yang, B. Honig, *J. Mol. Biol.* **1995**, *252*, 351–365.
[114] R. A. Friesner, J. L. Banks, R. B. Murphy, T. A. Halgren, J. J. Klicic, D. T. Mainz, M. P. Repasky, E. H. Knoll, M. Shelley, J. K. Perry, D. E. Shaw, P. Francis, P. S. Shenkin, *J. Med. Chem.* **2004**, *47*, 1739–1749.
[115] T. A. Halgren, R. B. Murphy, R. A. Friesner, H. S. Beard, L. L. Frye, W. T. Pollard, J. L. Banks, *J. Med. Chem.* **2004**, *47*, 1750–1759.
[116] G. Ferraro, L. Massai, L. Messori, A. Merlino, *Chem. Commun.* **2015**, *51*, 9436–9439.
[117] W. R. Algar, N. Hildebrandt, S. S. Vogel, I. L. Medintz, *Nat. Methods* **2019**, *16*, 815–829.
[118] F. R. Clemente, T. Vreven, M. J. Frisch in *Quantum Biochemistry*, Wiley, **2010**, pp. 61–83.
[119] T. Yanai, D. P. Tew, N. C. Handy, *Chem. Phys. Lett.* **2004**, *393*, 51–57.
[120] P. Fuentealba, H. Preuss, H. Stoll, L. Von Szentpály, *Chem. Phys. Lett.* **1982**, *89*, 418–422.
[121] S. Grimme, S. Ehrlich, L. Goerigk, *J. Comput. Chem.* **2011**, *32*, 1456–1465.
[122] A. K. Rappe, C. J. Casewit, K. S. Colwell, W. A. Goddard, W. M. Skiff, *J. Am. Chem. Soc.* **1992**, *114*, 10024–10035.
[123] A. R. Leach, B. K. Shoichet, C. E. Peishoff, *J. Med. Chem.* **2006**, *49*, 5851–5855.
[124] G. L. Warren, C. W. Andrews, A.-M. Capelli, B. Clarke, J. LaLonde, M. H. Lambert, M. Lindvall, N. Nevins, S. F. Semus, S. Senger, G. Tedesco, I. D. Wall, J. M. Woolven, C. E. Peishoff, M. S. Head, *J. Med. Chem.* **2006**, *49*, 5912–5931.
[125] K. M. Elokely, R. J. Doerksen, *J. Chem. Inf. Model.* **2013**, *53*, 1934–1945.

Manuscript received: February 9, 2023
Version of record online: June 7, 2023